Somatic tissue engineering in mouse models reveals an actionable role for WNT pathway alterations in prostate cancer metastasis

Josef Leibold[1*], Marcus Ruscetti[1*], Zhen Cao[2,3*], Yu-Jui Ho[1], Timour Baslan[1], Min Zou[4], Wassim Abida[5], Judith Feucht[6], Teng Han[3,7], Francisco M. Barriga[1], Kaloyan M. Tsanov[1], Leah Zamechek[1], Amanda Kulick[8], Corina Amor[1], Sha Tian[1], Katarzyna Rybczyk[1], Nelson R. Salgado[1], Francisco J. Sánchez-Rivera[1], Philip A. Watson[2], Elisa de Stanchina[8], John E. Wilkinson[9], Lukas E. Dow[7], Cory Abate-Shen[4], Charles L. Sawyers[2,10#], and Scott W. Lowe[1,10#]

[1]Department of Cancer Biology and Genetics, Memorial Sloan Kettering Cancer Center, New York, NY, USA.

[2]Human Oncology and Pathogenesis Program, Memorial Sloan Kettering Cancer Center, New York, NY, USA.

[3]Weill Cornell Graduate School of Medical Sciences, Weill Cornell Medicine, New York, NY, USA.

[4]Departments of Pharmacology, Urology, Medicine, Pathology and Cell Biology, and Systems Biology, Herbert Irving Comprehensive Cancer Center, Columbia University Medical Center, New York, NY, USA.

[5]Department of Medicine, Memorial Sloan Kettering Cancer Center, New York, NY, USA.

[6]Center for Cell Engineering and Immunology Program, Memorial Sloan Kettering Cancer Center, New York, NY, USA.

[7]Sandra and Edward Meyer Cancer Center, Department of Medicine, Weill Cornell Medicine, New York, NY, USA.

[8]Department of Molecular Pharmacology, Sloan Kettering Institute, Memorial Sloan Kettering Cancer Center, New York, NY, USA.

[9]Department of Pathology, University of Michigan, Ann Arbor, MI, USA.

[10]Howard Hughes Medical Institute, Chevy Chase, MD, USA.

[*]These authors contributed equally to this work.

[#]Corresponding Authors: Charles L. Sawyers, Memorial Sloan Kettering Cancer Center, 1275 York Avenue, Room C979, New York, NY, 10065. Phone: 646-888-2138; Email: sawyersc@mskcc.org; Scott W. Lowe, Memorial Sloan Kettering Cancer Center, 417 East 68th Street, Room ZRC 1104, New York, NY, 10065. Phone: 646-888-3342; Email: lowes@mskcc.org

RUNNING TITLE

Somatic tissue engineering in mice reveals mCRPC mechanisms

CONFLICTS OF INTEREST

W.A. received an honorarium from CARET, and is a consultant for Clovis Oncology, Janssen, MORE Health, and ORIC Pharmaceuticals. C.L.S. serves on the Board of Directors of Novartis, is a co-founder of ORIC Pharmaceuticals and co-inventor of enzalutamide and apalutamide. He is a science advisor to Agios, Beigene, Blueprint, Column Group, Foghorn, Housey Pharma, Nextech, KSQ, Petra, and PMV. S.W.L. is a co-founder and scientific advisory board member of Blueprint Medicines, ORIC Pharmaceuticals, Mirimus, Inc., Faeth Therapeutics, and Geras Bio, and is an advisor to Petra Pharmaceuticals, Constellation Pharmaceuticals, and Boehringer Ingelheim. L.E.D is an advisory board member for Mirimus Inc.

ABSTRACT

To study genetic factors influencing the progression and therapeutic responses of advanced prostate cancer, we developed a fast and flexible system that introduces genetic alterations relevant to human disease directly into the prostate glands of mice using tissue electroporation. These electroporation-based genetically engineered mouse models (EPO-GEMMs) recapitulate features of traditional germline models and, by modeling genetic factors linked to late stage human disease, can produce tumors that are metastatic and castration resistant. A subset of tumors with *p53* alterations acquired spontaneous WNT pathway alterations, which are also associated with metastatic prostate cancer in humans. Using the EPO-GEMM approach and an orthogonal organoid based model, we show that WNT pathway activation drives metastatic disease that is sensitive to pharmacological WNT pathway inhibition. Thus, by leveraging EPO-GEMMs, we reveal a functional role for WNT signaling in driving prostate cancer metastasis and validate the WNT pathway as therapeutic target in metastatic prostate cancer.

STATEMENT OF SIGNIFICANCE

Our understanding of the factors driving metastatic prostate cancer is limited by the paucity of models of late stage disease. Here, we develop electroporation-based genetically engineered mouse models (EPO-GEMMs) of prostate cancer and use them to identify and validate the WNT pathway as an actionable driver of aggressive metastatic disease.

INTRODUCTION

Prostate cancer is the most frequent cancer in American men and the second leading cause of their cancer-associated death (1). While localized disease is associated with an excellent prognosis, the 5-year survival rate drops dramatically in patients with metastatic prostate cancer from nearly 100% to 30%. Androgen deprivation therapy (ADT) has been the therapy of choice for prostate cancer patients for several decades (2); however, many patients that initially respond acquire resistance to ADT and eventually develop metastatic castration resistant prostate cancer (mCRPC).

Advanced prostate cancer is extensively characterized on the molecular level. In addition to androgen receptor (AR) amplification and activation of other AR pathway genes that are induced to bypass ADT, recent sequencing studies have identified various “non-canonical drivers” such as loss of *TP53*, amplification of *c-MYC* and *MYCN*, and alterations in the PI3K, WNT, and/or DNA repair pathways to be enriched in advanced prostate cancer (3-8). Yet, the potential functional role of many of these genetic alterations in driving either castration resistance or metastasis is unclear.

One way to study the functional role of various genetic perturbations in a physiological context is through the use of genetically engineered mouse models (GEMMs). While these models have been critical for our understanding of prostate cancer biology as well as for preclinical testing of new therapies (9), they lack the flexibility to test the impact of potential genetic drivers in a timely manner. GEMMs of prostate cancer have additional limitations: 1) many common genotypes are not represented; 2) most prostate-specific promoters used are androgen-dependent, making the study of androgen deprivation in these models difficult; 3) extensive intercrossing is needed to produce the alleles required for lethal disease; 4) tumor latency is long; 5) metastatic penetrance is often low; and 6) genes are frequently altered throughout the tissue leading to multi-focal tumors and potential effects of gene mutations on normal tissue that are not reflective of the human scenario.

In an effort to overcome these limitations, we took advantage of *in vivo* tissue electroporation (10-13) to produce somatic alterations directly in the prostate gland of otherwise wild type mice. We envisioned that this approach would produce focal prostate tumors of defined cancer genotypes, enabling the assessment of disease progression and/or therapy response in a physiological context in both a cost and time sensitive manner compared to that required for the production of multi-allelic germline strains. After validating the method in comparison to traditional GEMMs, we then used the EPO-GEMM approach to study genetic alterations associated with late-stage prostate cancer and confirmed our results with an orthogonal organoid based approach. These models identify WNT pathway alterations as actionable events that drive prostate cancer metastasis.

RESULTS

Somatic induction of oncogenic lesions by *in vivo* electroporation of the prostate gland

As a first attempt to produce prostate carcinoma in mice using tissue electroporation, we chose to introduce alterations leading to *MYC* overexpression and *PTEN* loss, which co-occur in advanced human prostate cancer and have been previously validated as prostate cancer drivers in mice (Figure S1A) (14,15). To this end, we performed a survival surgery to expose the prostate and delivered a plasmid cocktail containing 1) a transposon vector expressing a human *MYC* cDNA, 2) a Sleeping Beauty transposase (SB13), and 3) a gene editing vector co-expressing Cas9 and a single guide RNA (sgRNA) targeting *Pten* into one anterior lobe of the prostate of C57BL/6 male mice via *in vivo* electroporation (Figure 1A). While introduction of the transposon vector (to overexpress *MYC*) or the CRISPR/Cas9 vector (to edit *Pten*) alone did not produce tumors for up to one year post-electroporation, the combination was highly oncogenic, with lethal tumors arising with 83% penetrance and producing a median overall survival of 88 days (Figure 1B).

We compared the resulting tumor features to tumors arising in a classic GEMM model harboring *MYC* overexpression and a conditional *Pten* allele: *Nkx3.1*$^{CreERT2/+}$*;Pten*$^{fl/fl}$*;ARR2/Pbsn-MYC* (*NP*^{Hi}*MYC*) mice (Zou et al., in preparation) (14). As was noted in the germline model, *MYC;sgPten* (*MPt)* EPO-GEMM tumors harbored prostatic intraepithelial neoplasia (PIN) lesions (Figure S1B) together with regions of well-differentiated adenocarcinoma that expressed high levels of luminal markers AR and Cytokeratin 8 (CK8) and moderate levels of MYC and the proliferation marker Ki67 (Figures 1C, S1C, and S1D). Concurrently, many lesions contained adjacent poorly differentiated tumor regions with reduced to absent expression of AR and CK8, and a higher frequency of Ki67 compared to areas of well-differentiated adenocarcinoma (Figures 1D, S1C, and S1D). Occasionally, poorly differentiated areas also expressed the neuroendocrine (NE) marker Synaptophysin (SYP) (Figure 1D). As in the germline model, *MPt* EPO-GEMM tumors metastasized to lymph nodes, liver, and lungs (Figure S1E). *NP*^{Hi}*MYC* classic GEMM mice develop metastasis with higher penetrance than *MPt* EPO-GEMM mice (>80% vs. 54%), which is likely due to the accelerated rate of disease formation and death in the EPO-GEMM model (median survival >300 vs. 87.5 days) (Zou et al., in preparation) as well as differences in the genetic background of the mice. These results validate the EPO-GEMM platform as a fast and feasible system to model lethal, metastatic prostate cancer in mice.

Engineering advanced prostate cancer de novo using EPO-GEMMs

Alterations in the *TP53* tumor suppressor are rarely seen in early stages of prostate cancer but are amongst the most frequently altered genes in advanced disease (4,16), where they portend a particularly poor prognosis (17). *TP53* alterations also frequently co-occur with *MYC* amplifications in human prostate cancer patients (Figure S2A). We therefore tested whether the combination of *MYC* overexpression with *Trp53* (hereafter simply referred to as *p53*) disruption could lead to advanced prostate cancer in the EPO-GEMM platform (Figure S2B). While delivery of the *MYC*-containing transposon vector or plasmids expressing a *p53* sgRNA and Cas9 (to edit *p53*) alone did not lead to tumor formation up to one year after surgery, *MYC;sgp53* (*MP*) mice developed lethal prostate cancer as early as 64 days after electroporation, with 76% penetrance and a median survival of 114 days (Figure 2A). Macroscopically, primary tumors were identified in the anterior lobe of the prostate, and ~64% of the animals showed metastatic spread to the lymph nodes, peritoneum, liver or the lungs (Figures 2B). Of note, while disseminated tumor cells (DTCs) could be detected in the bone marrow using sensitive PCR approaches (Figure S2C), macroscopic bone metastasis was not observed using either histological or radiographic approaches (data not shown), suggesting that these genetic alterations might primarily lead to metastasis formation in soft tissues.

We next characterized the histological, biological and molecular features of *MP* prostate tumors. Both primary tumors and distant metastases consisted of poorly differentiated prostate cancer with low to absent expression of luminal markers AR and CK8, basal marker Cytokeratin 5 (CK5), and neuroendocrine marker synaptophysin, and high levels of MYC and Ki67 expression (Figures 2C and S2D). As *MP* tumors were mostly negative for both AR and NE markers (Figures 2C and S2D-F), they resemble "double negative" prostate cancer (DNPC), a subtype that has recently been described in human CRPC patients with increasing frequency and is enriched for alterations in *TP53* (18). Gene set enrichment analysis (GSEA) following RNA-sequencing revealed that, despite some heterogeneity in AR activity, the majority of *MP* tumors displayed low expression of AR and NE transcriptional signatures, consistent with DNPC (Fig. S2G) (19,20). In line with these findings, histological characterization of a human CRPC patient tumor harboring *MYC* and *TP53* alterations revealed heterogeneous areas that had high expression of luminal markers AR and CK8 or NE marker SYP, as well as others that showed low to absent expression of both AR and NE markers (i.e. DNPC) (Fig. S2H).

Since the EPO-GEMM approach does not *a priori* discriminate between cell types within a targeted tissue, we set out to confirm that the tumors we observed were derived from the epithelial compartment.

One powerful feature of the method is the ability to introduce somatic alterations into hosts of different genetic backgrounds to rapidly enable improved resolution of the target cell or, in principle, the study of tumor-host interactions. In one series of experiments, a plasmid encoding Cre recombinase was electroporated into the anterior prostate lobe of mice containing a Lox-Stop-Lox (LSL)-mKate cassette, and tissues were examined for mKate fluorescence in prostate luminal and basal cells. The results indicated that both epithelial cell types ($CK8^+$ luminal and $p63^+$ basal cells) were targeted by prostate electroporation (Figure S3A). In a second experiment, a *MYC* transposon vector and the Sleeping Beauty transposase together with a sgRNA targeting *p53* (sg*p53*) were delivered into the prostate of *Probasin* (*Pb*)-*Cre4;LSL-Cas9* mice, where only luminal or basal cells expressing Pb could undergo CRISPR/Cas9-mediated p53 editing (Figure S3B). Following electroporation, *Pb-Cre4;LSL-Cas9* mice yielded *MP* tumors with similar DNPC histological features and metastatic patterns as was observed in wild type (WT) C57BL/6 mice (Figures S3C-E), implying that prostate tumors driven by *MYC* overexpression and *p53* loss can originate from the epithelial compartment.

Human DNPC arises from prostate tumors that lose AR expression and therefore no longer display sensitivity to therapies targeting the AR signaling pathway (18,20). Accordingly, three independent prostate cancer cell lines generated from *MP* EPO-GEMM tumors showed only a marginal reduction in growth at a 10 μM therapeutic dose of the AR inhibitor enzalutamide as compared to the androgen-dependent Myc-CaP [generated from the MYC^{hi} mouse model (21,22)] and human LNCaP cell lines, which showed markedly reduced growth at lower concentrations of the drug (Figures 2D and S4A). Furthermore, while a modest yet statistically significant survival benefit was observed after surgical castration of a cohort of *MP* prostate tumor-bearing mice compared to the non-castrated cohort, all tumors continued to progress over a short one-week observation period (Figures 2E, S4B, and S4C). These data underscore the intratumoral heterogeneity of *MP* prostate tumors, with a subset of tumor cells remaining androgen sensitive but the majority becoming resistant to androgen deprivation.

TP53 mutant human cancers often harbor complex genomes with a high rate of copy number variations (CNVs) (23-25), which has been linked to metastasis formation and tumor relapse in prostate cancer (26). Similarly, murine *MP* tumors displayed a high rate of CNVs compared to *MPt* prostate tumors as assessed by sparse whole genome sequencing (Figure 2F). Among the gains and losses that were observed were alterations linked to late-stage disease, including recurrent amplifications in chromosome 3 (harboring *Pik3ca* and *Sox2)* and deletions in chromosome 14 (harboring the tumor suppressor *Nkx3.1*), as well as focal amplifications of *Ar* and *c-Jun* found in single tumors (Figures 2F and S4D-F) (4,5,27,28). Therefore, *MP* EPO-GEMM prostate tumors mirror the histological, castration-resistant, genomic instability, and metastatic features found in human prostate cancers with *TP53* mutations.

A subset of MYC/p53-driven tumors acquire WNT pathway activation

To further characterize the molecular features of *MP* tumors, we transcriptionally profiled a series of samples obtained from end-stage EPO-GEMM mice. RNA-sequencing followed by Principle Component Analysis (PCA) revealed that *MP* samples clustered into two distinct groups when compared to WT normal prostate or *MPt* prostate tumor samples (Figures 3A and S5A). Gene set enrichment analysis (GSEA) as well as gene ontology (GO) pathway analysis revealed that a WNT-β-catenin pathway signature was enriched in one of the *MP* clusters (Figures 3B, S5B, and S5C). In agreement, unsupervised clustering based on transcriptional expression of known WNT pathway genes bifurcated the *MP* samples into WNT high (WNT^{hi}) and WNT low (WNT^{lo}) groups (Figure 3C and S5D). Interestingly, WNT pathway activity appeared to correlate with the magnitude of metastatic spread, with WNT^{hi} tumors displaying a trend towards an overall greater frequency of metastasis, and in particular to the liver (Figures 3D and S5E), suggesting that deregulation of the WNT pathway may associate with prostate cancer metastasis.

Canonical WNT signaling is triggered by the binding of WNT ligands to WNT receptors such as LRP5/6, which results in the dismantling of the β-catenin destruction complex, leading to the translocation of β-catenin to the nucleus where it associates with the TCF family of transcription factors to activate WNT target genes (29). We therefore stained *MP* tumor sections for the expression of β-catenin and TCF7 as well as the presence of porcupine (PORCN), a O-Acyltransferase that is required for WNT ligand secretion and activation (30). β-catenin and TCF7 were elevated in WNT^{hi} *MP* tumors and associated with high levels of PORCN expression (Figures 3E, S5F, and S5G). In contrast, none of these factors were detectable in WNT^{lo} *MP* tumors.

WNT^{hi} tumors also expressed other molecular features consistent with WNT pathway activation. For example, our CNV analysis indicated that two WNT^{hi} *MP* samples harbored focal amplifications of *Lrp6*, a WNT receptor, and *Wnt2b*, a WNT ligand, which were associated with significant transcriptional upregulation of these genes (Figures 3F and S5G-I). Another tumor acquired a mutation in *Apc*, a negative regulator of the WNT pathway, corresponding to an event found (albeit rarely) in human tumors (Figure 3G). Interestingly, while *Apc* mRNA expression was reduced in both WNT^{hi} and WNT^{lo} *MP* tumors compared to normal murine prostate tissue, only WNT^{hi} tumors had induction of *Porcn* and a number of canonical WNT ligands (*Wnt 1, 2a, 2b, 10a, 10b*) (Figures 3C, S5G, and S5J). These data suggest that multiple factors contribute to WNT pathway activation in a subset of *MP* tumors.

WNT pathway alterations are associated with metastatic disease in patients with advanced prostate cancer

The link between WNT pathway activation and the more aggressive and metastatic disease identified in our EPO-GEMMs is in line with data from human prostate cancer patients (20). In a dataset of patients with either localized or advanced disease, *APC* mutations are most tightly associated with metastatic, non-castration resistant prostate cancer (5). Further inspection of datasets of human primary (TCGA

(31)) and metastatic (SU2C (3,4)) prostate cancer indicated that focal amplifications of *LRP5* and *LRP6* (also observed in one of our *MP* WNT^{hi} tumors) are associated with high transcriptional LRP5 and LRP6 activity and occurred at a significantly higher rate in metastatic prostate tumors than in localized disease (Figures 4A, 4B, S6A, and S6B). While alterations in *TP53* as well as *MYC* are associated with castration-resistant disease, mutations predicted to activate WNT signaling were enriched in patients with metastatic disease independently of castration-resistance status (Figures 4C-H). Overall, patients with prostate tumors harboring WNT pathway alterations showed a significantly higher metastatic frequency and reduced overall survival (Figures 4I and 4J) (3). Finally, when comparing primary prostate tumor biopsies from different patient cohorts, β-catenin expression (as a readout of WNT pathway activation) was higher in tumors from patients with metastatic compared to locoregional disease (Figures 4K and 4L).

WNT pathway activation promotes prostate cancer metastasis

To directly test whether WNT pathway alterations produce more aggressive and metastatic prostate cancers, we took advantage of the flexible EPO-GEMM platform to engineer tumors with constitutive WNT pathway activation. Specifically, we combined the *MYC* transposon vector with a dual CRISPR vector targeting *p53* as well as *Apc* at codon 892 (creating an N-terminal truncated protein) to generate *MPApc* EPO-GEMM mice (Figures S7A and S7B). As expected, the resulting tumors displayed evidence of both *p53* and *Apc* alterations, WNT pathway activation as assessed by abundant nuclear β-catenin and TCF7 expression, and all of the features of metastatic DNPC (Figures 5A and S7C-H).

Apc disruption also increased metastatic spread: 100% of *MPApc* mice developed distant metastases (19/19), as compared with ~64% of mice harboring *MP* prostate tumors (9/14) (Figures 5B and 5C). Furthermore, *MPApc* mice displayed a significantly reduced survival compared to *MP* cohorts (median survival 114 vs. 47 days) (Figure 5D). Moreover, the resulting *MPApc* tumors contained tumor regions with loss of E-cadherin and gain in Vimentin expression, indicative of an invasive, epithelial to mesenchymal transition (EMT)-like phenotype that has been previously associated with prostate cancer metastasis (Figure 5E) (32,33). Of note, a second *Apc*-targeting sgRNA predicted to produce a more central *Apc* truncation (at codon 1529) that recapitulates the most common *Apc* mutations found in human prostate cancer (Figure S8A) also activated WNT signaling and produced metastatic disease in 100% of the mice (Figures S8B-E). Furthermore, EPO-GEMM models produced with *MYC*, *Pten*, and *Apc* alterations (at codon 892) (*MPtApc*) displayed an increased frequency of metastasis compared to those with *MYC* and *Pten* alterations alone (100% vs. 54%) (Figure 5F-I and S8F). Therefore, distinct *Apc* truncations produce WNT pathway activation and promote metastasis in prostate cancers driven by multiple genetic configurations.

***Apc* mutations drive disease and metastatic progression in prostate cancer organoid models**

To validate the link between WNT pathway activation and prostate cancer metastasis in a well-defined orthogonal system, we created a series of mouse prostate organoids engineered to contain different genetic alterations. Starting from either sg*p53*-edited (hereafter referred to as $p53^{-/-}$) or $Pten^{-/-}$ (derived from *Pb-Cre; Pten*$^{flox/flox}$ mice) murine organoids, we engineered WNT pathway activation by CRISPR/Cas9-mediated genome editing of the *Apc* locus (hereafter referred to as $Apc^{-/-}$). Interestingly, constitutive WNT pathway activation through *Apc* disruption (at codon 892) in combination with *Pten* or *p53* deletion led to increased organoid growth as well as changes in organoid morphology *in vitro* (Figures S9A-D).

Orthotopic transplantation of $Pten^{-/-};Apc^{-/-}$ and $p53^{-/-};Apc^{-/-}$ organoids into immunodeficient NOD-*scid* IL2Rγ^{null} (NSG) mice led to a higher penetrance of tumor formation and enhanced tumor growth after 15 weeks compared to organoids harboring single gene alterations (Figures 6A and S9E). The resulting $p53^{-/-};Apc^{-/-}$ and $Pten^{-/-};Apc^{-/-}$ prostate tumors were histologically similar to *MPApc* and *MPtApc* EPO-

GEMM tumors, displaying poorly differentiated tumor regions that were low for AR and luminal markers CK8 and CK18, which was independently confirmed by immunoblotting for AR and AR targets FKBP5 and NKX3.1 (Figures 6B and S9F). Phenocopying the results in the EPO-GEMMs, these *p53*$^{-/-}$*;Apc*$^{-/-}$ and *Pten*$^{-/-}$*;Apc*$^{-/-}$ tumors also displayed an EMT-like phenotype containing regions with loss of E-cadherin and gain in Vimentin expression (Figure 6B).

Metastatic spread could not be assessed in the orthotopic transplantation model as mice succumb to tumor-induced urethral obstruction early on during tumor development. However, in a tail vein injection based assay, prostate organoids harboring an *Apc* mutation (*p53*$^{-/-}$*;Apc*$^{-/-}$ and *Pten*$^{-/-}$*;Apc*$^{-/-}$) produced observable lung metastasis 4 weeks after injection in contrast to their corresponding *Pten*$^{-/-}$ or *p53*$^{-/-}$ controls (Figure 6C). Similar results were obtained in *p53*$^{-/-}$ prostate organoids harboring a mutation in the central portion of the *Apc* gene at codon 1405 (*Apc*^{1405}) (Figures S9G-I). The increased metastatic capacity of *Apc* mutant tumors involved canonical WNT signaling, as shRNA-mediated *Ctnnb1* knockdown in organoids harboring *Apc* mutations completely ablated metastasis formation (Figure 6D). Together, these studies validate *Apc* mutations and WNT pathway activation as a driver of disease progression, invasion, and metastasis in prostate cancer.

Targeting WNT signaling disrupts prostate cancer metastasis

Owing to its deregulation in a plethora of other cancers (34,35), a number of pharmacological agents have been developed to block different components of the WNT signaling pathway. Small molecular inhibitors of the poly (ADP-ribose) polymerase Tankyrase stabilize Axin1 and increase phosphorylation and degradation of β-catenin, and have yielded promising preclinical results (36-39). Indeed, treatment with the tankyrase inhibitor G007-LK showed markedly decreased growth in all tested prostate cancer cell lines with high WNT activity compared to those without WNT pathway induction, including normal mouse fibroblasts (Figure 7A). Similar to results reported in a recent study exploring G007-LK efficacy in *Apc* mutant colon cancer (39), we found that prostate tumor cells harboring the central *Apc*^{1529} truncating mutant, which retains more of the β-catenin binding domain compared to the shorter N-terminal *Apc*^{892} mutant, were even more sensitive to the inhibitory effects of G007-LK treatment (Figure 7A). The drug produced molecular changes consistent with an on-target effect, as short-term G007-LK treatment of *MPApc* prostate cancer lines led to stabilization of Axin1 and increased phosphorylation of β-catenin; it also decreased WNT activity as measured by a decrease in the mRNA levels of Axin2, a WNT transcriptional target, and reduced TCF7 reporter activity (Figures S10A-C). These effects could be partially rescued by overexpression of the constitutively active S45P β-catenin mutant (Figures S10D and S10E).

The EPO-GEMM approach makes it feasible to generate large cohorts of mice that develop relatively synchronous tumors of a defined genotype, thereby providing a powerful system to test new treatment approaches in the preclinical setting. Therefore, we generated a series of *MPApc* EPO-GEMM mice (with *Apc* truncations at codon 892) and, upon tumor manifestation as assessed by ultrasound, randomized animals and treated cohorts with vehicle or G007-LK. Tankyrase inhibition produced a significant reduction in primary tumor growth and, importantly, reduced the occurrence of macrometastatic disease (Figures 7B and S10F). These effects produced a near doubling in lifespan of G007-LK-treated prostate tumor-bearing mice as compared to those in the vehicle-treated cohort (Figure 7C). Of note, while the reduction in metastasis observed following G007-LK treatment could arise indirectly from its inhibitory effects on primary tumors, G007-LK also prevented metastatic colonization in a tail vein injection assay (Figures 7D-F).

We also produced prostate tumors in mice following orthotopic transplantation of *MPApc*^{892} cells transduced with a WNT pathway reporter construct (TCF7-luciferase) and initiated treatment with G007-LK or vehicle control. In both the EPO-GEMM and orthotopic transplantation setting, tankyrase inhibition significantly decreased WNT pathway transcriptional activity *in vivo* as measured by a reduction in Axin2 mRNA levels and a decrease in 7TCF-luciferase activity following bioluminescent imaging (Figures S10G and S10H). Additionally, none of the G007-LK-treated mice had detectable metastases at the endpoint, whereas half of the mice in the vehicle-treated cohort did (Figures S10I and S10J).

Finally, to rule out the possibility that the anti-tumor effects of tankyrase inhibition were unique to tumors with engineered WNT pathway mutations, we produced orthotopic tumors from a 7TCF-luciferase expressing *MP* WNT^{hi} cell line and, upon tumor manifestation, mice were treated with vehicle or G007-LK (Figure 7G). As predicted from the above findings, G007-LK treatment reduced WNT transcriptional activity (Figures S10K and S10L) and reduced primary tumor growth as well as the frequency and number of lung and liver metastases (Figures 7H, 7I, and S10M-Q). Together, these data demonstrate that prostate tumors harboring WNT pathway alterations can acquire a dependency on WNT signaling that can be targeted therapeutically.

DISCUSSION

In this study we engineered and validated a non-germline GEMM (EPO-GEMM) that is flexible, efficient, and allows for the functional characterization of potential genetic drivers in prostate cancer. While traditional prostate cancer GEMMs are extraordinarily powerful, they are time-consuming and expensive, and typically require intercrossing of several germline strains to produce tumors that arise sporadically over long time periods. By contrast, the EPO-GEMM platform allows for the production of synchronized cohorts of mice harboring genetically defined tumors at a much greater speed and scale. For example, the *Nkx3.1*$^{CreERT2/+}$*;Pten*$^{fl/fl}$*;ARR2/Pbsn-MYC* GEMM requires intercrossing of least 4 germline alleles, producing only a small number of animals with the correct genotype that develop tumors after a much longer latency than the *MPt* EPO-GEMM model (319 vs. 87.5 day median survival)

(Zou et al, in preparation). Still, as with traditional GEMMs, EPO-GEMM models can recapitulate features of the human disease and, as shown here, *MP* tumors show features of 'double negative' castration resistant prostate cancer.

Beyond the increased speed associated with the approach, EPO-GEMMs have additional advantages compared to the traditional GEMMs. Similar to other somatic engineering approaches (40,41), the costs of EPO-GEMM models are minimal, requiring only the purchase of as many wild type mice as are needed to harbor the desired genotypes. As in human patients, tumors are focal and surrounded by normal tissue. Moreover, the models enable production of mice bearing tumors across a range of different genetic configurations in parallel, thereby facilitating their comparison. The relatively synchronous nature of tumor onset also enables the production of cohorts for preclinical studies. Tumors can also be engineered in any strain of mice, including those with alterations in particular stromal cell components, thereby enabling valuable studies of tumor-host interactions. Finally, the system is extremely portable, and in principle only requires sending plasmids and protocols to other laboratories. Some of the advantages of the EPO-GEMM system overlap with those achieved using the RapidCaP model (42), another strategy for somatic engineering of the prostate, though restrictions on the size and variety of vectors that can be used in that system limit its potential for producing genotypic diversity.

In this study, we took advantage of the unique features of the prostate EPO-GEMM approach to rapidly produce new genotypic configurations suggested from analysis of the original tumors, target different germline strains to establish the epithelial origin of the tumors, and generate synchronized cohorts of mice harboring genetically defined tumors for preclinical studies. Supporting the broad utility of this approach, others have used electroporation to produce cancers in the prostate and other organs (10-13). Other non-germline mouse modeling approaches, for example, organoid transplantation (40,43,44), stem cell manipulation/re-transplantation (45,46), and other somatic tissue engineering approaches (47,48) are continuing to make mouse models more accessible to the broader research community.

Using the EPO-GEMM approach, we identified WNT pathway activation as a potent contributor to aggressive and metastatic prostate cancer. Hence, a subset of *MP* prostate tumors spontaneously acquired signatures of WNT pathway activation. These tumors showed either genetic alterations or upregulation of genes capable of activating WNT signaling. Data from genomic studies of human prostate cancer identified *APC* mutations as prominently associated with metastatic prostate cancer and, consistent with our findings, further analyses linked previously undescribed amplifications of the WNT co-receptors *LRP5* and *LRP6* to metastatic disease in patients. Leveraging both the EPO-GEMM platform and an orthogonal organoid transplantation approach, we showed that disruption of the *Apc* tumor suppressor by modeling human-relevant mutations could drive aggressive and metastatic disease – a link that has not previously been confirmed in traditional GEMMs (49,50). Finally, we demonstrated that a tankyrase inhibitor could repress WNT signaling, reduce metastasis, and improve overall survival.

Whereas a recent study demonstrated that *p53* loss directly leads to the secretion of WNT ligands that contribute to breast cancer metastasis by driving systemic inflammation (51), the contribution of *p53* loss and WNT pathway activation to prostate cancer progression in our model is distinct: here, *p53* loss drives progression to aggressive CRPC, and, perhaps by conferring inherent genomic instability, enables the acquisition of genetic and transcriptional alterations in the WNT pathway that converge to drive metastasis. Though we did not identify a specific WNT ligand or receptor necessary for pathway activation, we found that PORCN, which is required for proper WNT ligand processing and secretion, was commonly induced only in WNT activated tumors, suggesting that an increase in autocrine/paracrine WNT signaling is driving pathway activity. Differences in cell-of-origin may also contribute to these heterogeneous mechanisms of WNT pathway activation, as well as possibly explain why we see WNT activity in some tumors but not others.

Importantly, alterations in *Apc* are also sufficient to promote metastasis irrespective of the *p53* (or *MYC*) genomic status, since *MPtApc* EPO-GEMMs and *Pten*$^{-/-}$;*Apc*$^{-/-}$ organoid transplant prostate tumors also displayed an increased rate of metastasis. Moreover, *Apc* altered prostate organoids displayed enhanced metastatic progression in immunodeficient hosts, indicating that WNT pathway activation can drive metastasis formation in prostate cancer independently of its role in mediating systemic inflammation. Notably, we identified markers associated with an EMT, a phenotype which has previously been linked to the acquisition of invasive and stemness characteristics and metastasis formation in prostate cancer (32,33,52), in tumors following WNT pathway activation, thus providing a potential mechanism of how WNT pathway activation stimulates metastatic spread. Collectively, our results functionally validate clinical associations between WNT pathway alterations, metastasis, and poor survival in CRPC patients (3,6) (Figure 4).

Our results also demonstrate that WNT pathway activation can confer an actionable vulnerability in the setting of mCRPC. Indeed, tumor cells harboring WNT pathway activation displayed enhanced sensitivity to tankyrase inhibition *in vitro* and *in vivo*, and our data support the notion that those tumors harboring central *Apc* truncations or alterations in WNT ligands/receptors, which are collectively the most common WNT pathway alterations found in human CRPC, will be the most sensitive to its effects. While we cannot rule out the possibility that some of the anti-tumor effects produced by G007-LK result from off-target effects on stromal cells, the ability of tankyrase inhibition to impede WNT signaling in tumor cells *in vivo*, and its selective effects on WNT altered tumor cells *in vitro*, support the notion that these effects arise, at least in part, from inhibiting WNT signaling in tumor cells themselves. Beyond this, our observation that LRP5/6 amplifications are common in human metastatic prostate cancer raise the possibility that these tumors will also be sensitive to PORCN inhibition or other upstream WNT pathway antagonists. While dose-limiting toxicities may preclude sufficient tankyrase inhibition in patients, our results provide proof-of-concept that WNT pathway alterations can produce actionable dependencies in prostate cancer. As therapeutic options are limited in this advanced stage of the disease, inhibition of the WNT pathway might be a valid strategy to treat mCRPC patients.

METHODS

Cell culture and compounds

LNCaP and Myc-CAP cells were provided by P.A. Watson. Primary murine fibroblasts from C57BL/6 mice were purchased from Cell Biologics, Inc and grown in complete fibroblast media (M2267). *MPt*, *MP*, and *MPApc* murine prostate cancer cell lines were derived from EPO-GEMM prostate tumors with these genotypes. To generate these cell lines, prostate tumors were minced, digested in DMEM media containing 3 mg/ml Dispase II (Gibco) and 1 mg/ml Collagenase IV (C5138;Sigma) for 1 hour at 37°C, and plated on 10 cm culture dishes coated with 100 µg/ml collagen (PureCol) (5005; Advanced Biomatrix). Primary cultures were passaged at least 3 times to remove fibroblast contamination. All prostate cancer cell lines were maintained in a humidified incubator at 37°C with 5% CO_2, and grown in RPMI 1640 or DMEM supplemented with 10% FBS and 100 IU ml^{-1} penicillin/streptomycin. All cell lines used were negative for mycoplasma.

Enzalutamide (S1250) and G007-LK (S7239) were all purchased from Selleck chemicals for *in vitro* studies. Drugs for *in vitro* studies were dissolved in DMSO (vehicle) to yield 10 mM stock solutions and stored at -80°C. For *in vitro* studies, growth media with or without drugs was changed every 3 days. For *in vivo* studies, G007-LK (B5830) was purchased from APExBIO. G007-LK was dissolved in 10% DMSO and then reconstitued in 20% Cremophor EL (Sigma-Aldrich) in saline.

In vitro genome editing

For visualizing WNT pathway activity *in vivo*, *MP* and *MPApc* cell lines were engineered to express a 7TCF-Luciferase construct (a gift from Roel Nusse (Addgene plasmid # 24308)). Lentivuruses were packaged by co-transfection of Gag-Pol expressing 293 T cells with expression constructs and envelope vectors (VSV-G) using the calcium phosphate method. Following transduction, cells were selected with 4µg/ml puromycin for 1 week.

MiRE-based shRNAs targeting *Apc*, *Ctnnb1*, and *Renilla* were cloned into MSCV-based vectors as previously described (53,54). Retroviruses were packaged by co-transfection of Gag-Pol expressing 293 T cells with expression constructs and envelope vectors (VSV-G) using polyethylenimine (PEI; Sigma-Aldrich). Following transduction with shRNA retroviral constructs, cell selection was performed with 4µg/ml puromycin for 1 week. Perturbation of WNT pathway activity following *Apc* or *Ctnnb1* knockdown was confirmed by qRT-PCR or readout of TCF activity through TOPFLASH assays.

Plasmids containing a mutant form of β-catenin (βcat^{S45P}) were provided by L. Dow. To engineer *MPApc* cell lines to express βcat^{S45P}, retroviruses were packaged by co-transfection of Gag-Pol expressing 293 T cells with expression constructs and envelope vectors (VSV-G) using PEI. Following transduction, cells were selected with 4µg/ml puromycin for 1 week.

Establishment of organoid lines

Mouse prostate organoids were established and cultured as described previously (55). $Pten^{-/-}$ organoids were established from *Pb-Cre; Pten*$^{flox/flox}$ mice. WT or $Pten^{-/-}$ organoids were transduced with lentiCas9-Blast and the bulk population was selected in blasticidin for 3 days. WT organoids were then transduced with LentiCRISPRv2-sgp53 and bulk selected in puromycin for 3 days to generate $p53^{-/-}$ organoids. *Apc* mutant organoid lines were generated using Retro-sgApc-tdTomato constructs targeting codons 884 and 1405 (provided by T. Han and L. Dow) and were bulk sorted to enrich for transduced cells as previously described (56). *Ctnnb1* knockdown was achieved using MiRE-based shRNAs targeting *Ctnnb1* as described above.

In vitro organoid growth analysis

Organoid growth analysis was carried out as previously described (57). 1,000 cells per 50 µl matrigel dome were seeded in EGF withdrawal medium, and each time point consisted of 3 domes in a 24-well plate. Cell viability was assessed using the CellTiter-Glo Viability Assay (Promega) according to the manufacturer's protocol. All values for each time point were normalized to day 1 readings.

Animal studies

All mouse experiments were approved by the Memorial Sloan-Kettering Cancer Center (MSKCC) Internal Animal Care and Use Committee. Mice were maintained under specific pathogen-free conditions, and food and water were provided ad libitum. Mice were purchased from Jackson laboratory. *Pb-Cre4* (58) male mice were crossed with *LSL-Cas9* female mice to produce *Pb-Cre4;LSL-Cas9* male mice for generation of EPO-GEMMs.

Electroporation-induced genetically engineered mouse models (EPO-GEMMs).

8-12 week old WT C57BL/6, or transgenic *Pb-Cre;LSL-Cas9* and *Rosa26-CAGs-LSL-RIK* (59) male mice were anesthetized with isofluorane and the surgical site (pelvic region) scrubbed with a povidone-iodine scrub (Betadine) and rinsed with 70% alcohol. After opening the peritoneal cavity, the left seminal vesicle was used as a landmark and the left anterior lobe of the prostate was pulled out. 50 µl of a plasmid mix (see specifications below) was injected into the left anterior lobe of the prostate using a 27.5 gauge syringe and tweezer electrodes were tightly placed around the injection bubble. Two pulses of electrical current (60V) given for 35 ms lengths at 500 ms intervals were then applied using an *in vivo* electroporator (NEPAGENE NEPA21 Type II electroporator). After electroporation, the peritoneal cavity was rinsed with 0.5ml of pre-warmed saline. After the procedure the peritoneal cavity was sutured and the skin closed with skin staples. The mice were kept at 37˚C until they awoke and post-surgery pain management was done with injections of buprenorphine and/or meloxicam for the three following days. Tumor formation was assessed by ultrasound imaging, and mice were sacrificed following early tumor development or at endpoint. Genome editing in EPO-GEMM tumors was confirmed by Sanger sequencing.

To generate EPO-GEMM tumors in C57BL/6 WT mice, the following vectors and concentrations were used: a pT3-MYC transposon vector (5µg), a Sleeping Beauty transposase (SB13) (1µg), and/or a pX330 CRISPR/Cas9 vector (20µg) (addgene #42230) targeting the respective tumor suppressor genes. For generation of tumors in *Pb-Cre;LSL-Cas9* mice, a pT3-MYC transposon vector (10µg) (addgene #92046), pT3-sgp53 transposon vector (20µg), and SB13 (6µg) were used. For assessment of tissue recombination in *Rosa26-CAGs-LSL-RIK* mice, a PGK-Cre vector (10µg) was used. The Sleeping Beauty transposase (SB13) and the pT3 transposon vector were a generous gift of Dr. Xin Chen, UCSF San Francisco. The pX330 vector was a gift from Feng Zhang (addgene plasmid # 42230).

The following sgRNAs were used to target the respective tumor suppressor gene locus:

Pten: GTTTGTGGTCTGCCAGCTAA
p53: ACCCTGTCACCGAGACCCC
Apc^{892}: CAGGAACCTCATCAAAACG
Apc^{1529}: CAGTTCAGGAAAACGACAA
Apc^{1405}: GTTCAGAGTGAGCCATGTAG

To generate the pX330 vector containing two sgRNAs, the vector was opened using the XbaI cloning site and the sgRNA-casette containing the second guide was PCR cloned into the vector using the following primers: XbaI U6 fwd. ATGCTTCTAGAGAGGGCCTATTTCCCATGATT and NheI gRNA scaffold rev. ATGTCGCTAAGCTCTAGCTCTAAAACAAAAAAGC.

Ultrasound imaging

High-contrast ultrasound imaging was performed on a Vevo 2100 System with a MS250 13- to 24-MHz scanhead (VisualSonics) to stage and quantify prostate tumor burden. Tumor volume was analyzed using Vevo LAB software.

Bioluminescence imaging

Bioluminescence imaging (BLI) was used to track luciferase expression in orthotopically transplanted *MPApc* or *MP* WNT^{hi} prostate cell line tumors expressing a 7TCF-Luciferase (Luc) reporter, as well as orthotopically and intravenously transplanted organoids expressing a Luc reporter. Mice were injected i.p. with luciferin (5 mg/mouse; Gold Technologies) and then imaged on a Xenogen IVIS Spectrum imager (PerkinElmer) 10-15 minutes later for 60 seconds. Quantification of luciferase signaling was analyzed using Living Image software (Caliper Life Sciences).

Orthotopic transplantation of cell lines

50,000 *MPApc* or *MP* WNT^{hi} prostate tumor cells expressing a 7TCF-Luc reporter were resuspended in 25 µl of a 50% matrigel (BD Biosciences)/ 50% PBS solution and injected into the right anterior prostate lobe of 8-10 week old male C57BL/6 mice using a Hamilton Syringe as previously described (52). BLI imaging was used to assess tumor formation, and mice were subsequently randomized and enrolled into treatment groups. The impact on metastatic burden was assessed after four weeks of treatment.

In vivo metastasis assay using cell lines

500,000 *MP* or *MPApc* prostate tumor cells were resuspended in 400 µl of PBS and tail vein injected into 8-10 week old *Nu/Nu* (Nude) male mice.

Orthotopic transplantation of organoids

A LentiLuciferase-Neo construct was transduced into all organoid lines and bulk selected for 3 days in neomycin. 3 x 10^6 cells per mouse were used for orthotopic injection. Organoids were dissociated into single cells and resuspended in 50% matrigel and 50% medium before injection into NOD-*scid* IL2Rγ^{null} (NSG) male mice. *In vivo* luciferase signals were measured once a week on an IVIS Spectrum imager. Mouse prostate tissues were collected after 13 weeks for histological analysis.

In vivo metastasis assay using organoids

25,000 dissociated LentiLuciferase-Neo transduced orgnaoid cells were resuspended in 400 µl of PBS and tail vein injected into NSG mice. *In vivo* luciferase signals were measured once a week on an IVIS Spectrum imager. Mouse lung tissues were collected 40 days post-injection.

Surgical castration

Castration was performed as previously described (60). EPO-GEMM mice were monitored for prostate tumor development by ultrasound, and enrolled and randomized into treatment groups once tumors reached 500 mm^3. Ultrasound imaging was repeated every week following castration to assess changes in prostate tumor burden. Upon sacrifice prostate tumor tissue was allocated for 10% formalin fixation and OCT frozen blocks.

Pre-clinical treatment studies

EPO-GEMM mice were monitored for prostate tumor development by ultrasound, and enrolled and randomized into treatment groups once tumors reached 500 mm^3. C57BL/6 mice orthotopically transplanted with *MP* and *MPApc* prostate tumors cells expressing a 7TCF-Luc reporter were evaluated by BLI to verify tumor development before being randomized into various study cohorts. Nude mice tail vein injected with *MPApc* prostate tumor cells were randomized and treated either with G007-LK or vehicle control the day before injection to assess metastasis prevention.

Mice were treated with vehicle or G007-LK (30 mg/kg body weight) by intraperitoneal (ip) injection for 5 consecutive days followed by 2 days off treatment. Ultrasound and/or BLI were repeated every week during treatment to assess changes in prostate tumor burden. No obvious toxicities were observed in vehicle- or drug-treated animals as assessed by changes in body weight. Upon sacrifice prostate tumor tissue was allocated for 10% formalin fixation and snap frozen tissue for DNA/RNA analysis.

Analysis of metastasis burden

The presence of peritoneal, lymph node, thorax, lung, and liver metastases was determined at survival or experimental endpoint by gross examination under a dissecting scope. Metastasis burden and the total number of individual metastases was further quantified from H&E stained sections. The presence of disseminated tumors cells (DTCs) in the bone marrow of EPO-GEMM mice was assessed following PCR genotyping for the presence of the human *MYC* allele in the bone marrow flushes from the hindlimbs of these mice. PCR genotyping of *MP* EPO-GEMM prostate tumors and normal WT prostate tissue were used as positive and negative controls, respectively.

Immunohistochemistry and immunofluorescence

Tissues were fixed overnight in 10% formalin, embedded in paraffin, and cut into 5 μm sections. Haematoxylin and eosin (H&E) and immunohistochemical/immunoflourescence staining was performed using standard protocols. The following primary antibodies were used: Androgen Receptor (AR; Sc-816), p63 (Sc-8431), and CK8 (Sc-8020) (Santa Cruz); Porcupine (PORCN; AB105543), MYC (AB32072), Ki67 (AB16667), and LRP6 (AB24386) (Abcam); Cytokeratin 5 (CK5; 905501) and Cytokeratin 8 (CK8; 904801) (Biolegend); β-catenin (BD610153), E-cadherin (BD610181), and ASCL1 (MASH1;BD556604) (BD Biosciences); Synaptophysin (SYP; 1485-1) (Epitomics); mKate2 (AB233) (Evrogen); p63 (4A4, Ventana); Vimentin (5741), and TCF1/TCF7 (2203) (Cell Signaling). Histopathological features in EPO-GEMM primary prostate tumors and metastases were assessed by a trained veterinary pathologist (J. Wilkinson).

High throughput RNA-sequencing (RNA-seq)

For RNA-seq analysis of the transcriptional profiles of *MPt* and *MP* EPO-GEMM prostate tumors, as well as normal anterior lobe tissue from prostates of wild type (WT) C57BL/6, total RNA was extracted from bulk tissue using the RNeasy Mini Kit (Qiagen). Purified polyA mRNA was subsequently fragmented, and first and second strand cDNA synthesis performed using standard Illumina mRNA TruSeq library preparation protocols. Double stranded cDNA was subsequently processed for TruSeq dual-index Illumina library generation. For sequencing, pooled multiplexed libraries were run on a HiSeq 2500 machine on RAPID mode. Approximately 10 million 76bp single-end reads were retrieved per replicate condition. Resulting RNA-Seq data was analyzed by removing adaptor sequences using Trimmomatic (61), aligning sequencing data to GRCm38.91(mm10) with STAR (62), and genome wide transcript counting using featureCounts (63) to generate a TPM matrix of transcript counts. Genes were identified as differentially expressed using R package DESeq2 with a cutoff of absolute $\log_2$FoldChange ≥ 1 and adjusted p-value < 0.05 between experimental conditions (64). Functional enrichments of these differentially expressed genes were performed with enrichment analysis tool Enrichr (65) and the retrieved combined score (log(p-value) * z-score) was displayed.

Clustering and Gene Set Enrichment Analysis (GSEA)

Principal component analysis was performed using the DESeq2 package in R. Gene expressions of RNA-Seq data were clustered using hierarchical clustering based on one minus pearson correlation test. For pathway enrichment analysis, the weighted GSEA Preranked mode was used on a set of curated signatures in the molecular signatures database (MSigDB v7.0) (http://www.broadinstitute.org/gsea/msigdb/index.jsp). From 22,596 signatures, signatures with 15-500 genes were only considered for further analyses. From the results, enriched signatures with an adjusted *p* value less than 0.05 were considered as statistically significant.

Copy Number Variations (CNVs)

CNVs were infered from sparse whole genome sequencing data as described previously (66,67). In brief, 1 µg of bulk genomic DNA (gDNA) was extracted from prostate tumors and tissue using the DNeasy Blood & Tissue Kit (Qiagen) and sonicated using the Covaris instrument. Sonicated DNA was subsequently end-repaired/A-tailed, followed by ligation of TruSeq dual indexed adaptors. Indexed libraries were enriched via PCR and sequenced in multiplex fashion using the Illumina HiSeq2500 instrument to achieve roughly 1 million uniquely mappable reads per sample – a read count sufficient to allow copy number inference to a resolution of approximately 400kb. For data analysis, uniquely mapped reads where counted in genomic bins corrected for mappability. Read counts were subsequently corrected for GC content, normalized, and segmented using Circular Binary Segmentation (CBS). Segmented copy number calls are illustrated as relative gains and losses to the median copy number of the entire genome. Broad events (chromsome wide and several megabase sized events) are discernible in a genome-wide manner as illustrated in Figure 2F. Focal events, namely chromsomal amplifications, are discernible in zoom-in-views of chromosomes as depicted in Figures 3F, S4D, and S4E.

Mouse MSK-IMPACT

Tumors were profiled for genomic alterations in M-IMPACT_v1key cancer-associated genes using our custom, deep sequencing MSK-IMPACT assay that surveys 468 known cancer driver genes. Custom DNA probes were designed for targeted sequencing of all exons and selected introns of oncogenes, tumor suppressor genes, and members of pathways deemed actionable by targeted therapies. Genomic DNA from tumor and matched normal WT prostate anterior tissue samples were subjected to sequence library preparation and exon capture (NimbleGen). Up to 30 barcoded sequence libraries were pooled at equimolar concentrations and input into a single exon capture reaction, as previously described (68). Pooled libraries containing captured DNA fragments were subsequently sequenced on the Illumina HiSeq system.

Sequence data were demultiplexed using BCL2FASTQv1.8.3 (Illumina), and vesitigial adapter sequences were removed from the 3' end of sequence reads. Reads were aligned in paired-end mode to the hg19 b37 version of the genome using BWA-MEM (Burrows-Wheeler Alignment tool). Local realignment and quality score recalibration were performed using Genome Analysis Toolkit (GATK) according to GATK best practices (69). Paired-sample variant calling was performed on tumor samples and their respective matched normals to identify point mutations/single nucleotide variants (SNVs) and small insertions/deletion (indels). MuTect (version 1.1.4) (70) was used for SNV calling and SomaticIndelDetector, a tool in GATKv.2.3.9, was used for detecting indel events. Variants were subsequently annotated using Annovar, and annotations relative to the canonical transcript for each gene (derived from a list of known canonical transcripts obtained from the UCSC genome browser) were reported.

Tissue microarray (TMA)

Tissue microarrays (purchased from US Biolab) containing a total of 126 prostate tumor specimens from 66 patients with localized and metastastic disease were stained for β-catenin expression by immunofluorescence through the Molecular Cytology Core Facility at MSKCC using a Discovery XT processor (Ventana Medical Systems). Briefly, tissue sections were deparaffinized with EZPrep buffer (Ventana Medical Systems) and antigen retrieval was performed with CC1 buffer (Ventana Medical Systems). Sections were blocked for 30 minutes with Background Buster solution (Innovex), followed by avidin-biotin blocking for 8 minutes (Ventana Medical Systems). Sections were incubated with a β-catenin antibody (8814; Cell Signaling) for 5 hours, followed by a 60-minute incubation with biotinylated goat anti-rabbit IgG (PK6101; Vector labs) at a 1:200 dilution. Detection was performed with Streptavidin-HRP D (part of DABMap kit, Ventana Medical Systems), followed by incubation with Tyramide Alexa 488 (B40953; Invitrogen) prepared according to the manufacturer's instructions. After staining, slides were counterstained with DAPI (D9542; Sigma Aldrich) for 10 min and coverslipped with Mowiol. Tissues were then scored on a 0-3 scale for β-catenin expression, with scores of 0 and 1 as "negative" and 2 and 3 as "positive" for β-catenin.

Human clinical data analysis

CBioPortal.org was used to plot the frequency of mutations, amplifications, and/or deletions in genes of interest in prostate cancer patients from various datasets. *TP53* alterations included deep deletions (homozygous loss) as well as missense, inframe, and truncating mutations. A Kaplan-Meier survival curve of prostate cancer patients with or without WNT pathway alterations was generated using part of the SU2C dataset (3), which included 47 patients in the WNT activated group and 81 patients in the non-WNT activated group. Patients were randomized into the two groups based on WNT pathway activating alterations in the following genes: *CTNNB1, APC, AXIN2, WIF1, SFRP1, DKK1, RNF43, ZNRF3, GSK3B, TCF7, TLE1, LRP5, LRP6,* and *WNT2b* (71). The percentage of WNT pathway altered prostate tumor specimens from patients with locoregional vs. metastatic disease was determined from an MSK-IMPACT dataset (5), which included 194 locoregional, 135 mPC, and 147 mCRPC patients. Locoregional disease in this setting indicated disease without distant clinical or pathologic spread, including lymph node involvement in the pelvis only. *LRP5* and *LRP6* amplification frequency was determined from a dataset containing samples obtained from primary tumors where CNV analysis was performed by Affymetrix SNP 6.0 (31), or two datasets containing samples obtained from metastatic sites where CNV analysis performed by whole exome sequencing (3,4). *LRP5* and *LRP6* expression levels in amplified (AMP or GAIN) or non-amplified tumors were determined in mCRPC patients samples from the SU2C dataset (3) using normalized fpkm values and CNV calls.

Patients and Samples

Histopathological analysis was performed on a primary prostate tumor tissue biopsy from a mCRPC patient treated at MSKCC harboring a *MYC* amplification and p53 alteration (L114Ffs*33) as part of the MSK-IMPACT cohort (5,72). Clinical sequencing analysis (MSK-IMPACT) was completed on this and other samples and collected using a web-based electronic data capture. Immunohistochemical and sequencing analysis on human tissue samples were performed under MSKCC Institutional Review Board approval. All samples and clinical data were deidentified.

AR^+, NE^+, and DN PC classification

We adhered to the AR^+/NE^+/DN prostate cancer subtype classification as proposed in (18). Briefly, AR and NE scores were calculated according to the expression of the mRNA z-scores of 10 AR activity genes (KLK3, KLK2, TMPRSS2, FKBP5, NKX3-1, PLPP1, PMEPA1, PART1, ALDH1A3, STEAP4) and 10 NE signature genes (SYP, CHGA, CHGB, ENO2, CHRNB2, SCG3, SCN3A, PCSK1, ELAVL4, NKX2-1) for mouse and human prostate samples (19). Subsequently, samples for each dataset were normalized from 1 (highest expression of either NE or AR score, respectively) to 0 (lowest expression of either NE or AR score, respectively) as displayed in the scattered plot. Immunohistochemical staining and quantification of AR and SYP/ASCL1 (NE) marker expression was also used for subtype classification in some mouse and human tumors. DN prostate cancers were defined as those that lacked expression of both AR^+ and NE^+ markers.

TOPFLASH Assay

10,000 cells were plated in 100 µl of media containing 10% FBS per well of a black-walled 96-well plate (Perkin Elmer). After 24 hours, cells were transfected using PEI with 170 ng of TOPFLASH Firefly reporter and 30 ng of pRL-SV40P *Renilla* constructs provided by T. Tamella. In initial experiments, the WNT-insensitive FOPFLASH Firefly reporter (also provided by T. Tamella) was used to rule out signal background (not shown). 36 hours after transfection, *Firefly* and *Renilla* signals were detected using Dual-Glo luciferase detection reagents (Promega) according to manufacturer's instructions. A Varioskan Flash plate reader (Thermo Fischer Scientific) was used to detect luminescence. To control for transfection efficiency, Firefly luciferase levels were normalized to *Renilla* luciferase levels to generate the measure of relative 7TCF activity.

Immunoblotting

Cell lysis was performed using RIPA buffer (Cell signaling) supplemented with phosphatase inhibitors (5mM sodium fluoride, 1 mM sodium orthovanadate, 1 mM sodium pyrophosphate, 1 mM β-glycerophosphate) and protease inhibitors (Protease Inhibitor Cocktail Tablets, Roche). Protein concentration was determined using a Bradford Protein Assay kit (Biorad). Proteins were separated by SDS-PAGE and transferred to polyvinyl difluoride (PVDF) membranes (Millipore) according to standard protocols. Membranes were immunoblotted with antibodies against Axin1 (2087), phospo-β-catenin S33/S37/T41 (9561), PTEN (9188), P53 (2524), and FKBP5 (12210) from Cell Signaling, AR (ab108341), cyclophilin B (ab16045), and NKX3.1 (ab196020) from Abcam, APC (OP44) from Millipore, and P21 (sc-6246) from Santa Cruz in 5% BSA in TBS blocking buffer. After primary antibody incubation, membranes were probed with an ECL anti-rabbit IgG or anti-mouse IgG secondary antibody (1:10,000) from GE Healthcare Life Science and imaged using a FluorChem M system (Protein Simple). Protein loading was measured using a monoclonal β-actin antibody directly conjugated to horseradish peroxidase (1:20,000) from Sigma-Aldrich and imaged as above.

qRT-PCR

Total RNA was isolated using the RNeasy Mini Kit (Qiagen), and complementary DNA (cDNA) was obtained using the TaqMan reverse transcription reagents (Applied Biosystems). Real-time PCR was performed in triplicate using SYBR Green PCR Master Mix (Applied Biosystems) on the ViiA 7 Real-Time PCR System (Invitrogen). GAPDH and mRn18s served as endogenous normalization controls.

Cell viability assay

5,000 cells were plated in 100 µl of media containing 10% FBS per well of a black-walled 96-well plate (Perkin Elmer). The next day the media was changed, and cells were treated with G007-LK or enzalutamide for 72 hours. Following treatment, cell viability was assessed using the CellTiter-Glo Viability Assay (Promega) according to the manufacturer's protocol. IC_{50} calculations were made using Prism 6 software (GraphPad Software).

Statistical analysis

Statistical analyses were performed as described in the figure legend for each experiment. Group size was determined on the basis of the results of preliminary experiments and no statistical method was used to predetermine sample size. The indicated sample size (*n*) represents biological replicates. Group allocation and outcome assessment were not performed in a blinded manner. All samples that met proper experimental conditions were included in the analysis. Survival was measured using the Kaplan–Meier method. Statistical significance was determined by one- and two-way ANOVA, Fisher's exact test, Student's t test, log-rank test, Mann-Whitney test, and Pearson's correlation using Prism 6 software (GraphPad Software) as indicated. Significance was set at $P < 0.05$.

Data Availability

RNA-seq data generated in this study are deposited in the Gene Expression Omnibus database under accession number GSE139340. Mouse IMPACT sequencing data presented in this study are deposited in the NCBI BioProject database under accession number PRJNA610252.

Figure Preparation

Figures were prepared using BioRender.com for scientific illustrations and Illustrator CC 2020 (Adobe).

ACKNOWLEDGEMENTS

We thank T. Tammela and O. Grbovic-Huezo for sharing tissue samples; E.M. Schatoff for sharing reagents, plasmids, and experimental protocols; N. Socci and the Bioinformatics Core for assistance with Mouse IMPACT sequencing analysis; F. Sanchez-Vega and N. Schultz for assistance with genomic analysis of human datasets; A. Tehuitzil, A. Wuest, A. Kim, C.J. Hagen, D. Choi, A.C. Agudelo Rivera, and A. Gaglio for technical assistance; C.J. Sherr and H. Wu for helpful comments on the manuscript; and other members of the Lowe laboratory for insightful discussions. We thank Mr. William H. and Mrs. Alice Goodwin and the Commonwealth Foundation for Cancer Research for research support. This work was also supported by a P50 CA092629 Prostate Cancer Spore grant (S.W.L.), a Memorial Sloan Kettering Cancer Center Support grant (P30 CA008748), National Institutes of Health (NIH) grants (R01 CA155169, CA193837, CA224079, CA092629, and CA160001 to C.L.S., CA233944 and CA087497 to S.W.L, U54 OD020355 to S.W.L. and E.d.S, and R01 CA183929 and CA173481 to C.A.S.), Starr Cancer Consortium grants I10-0062 and I12-0007 (C.L.S.), and an Agilent Thought Leader Award (S.W.L.). S.W.L. is the Geoffrey Beene Chair for Cancer Biology, and S.W.L. and C.L.S. are investigators in the Howard Hughes Medical Institute (HHMI). We also acknowledge support to J.L. from the German Research Foundation (DFG) and the Shulamit Katzman Endowed Postdoctoral Research Fellowship, to M.R. from the American Cancer Society (PF-16-115-01-TBG) and the NCI (K99 CA241110), to T.B. from the William C. and Joyce C. O'Neil Charitable Trust and Memorial Sloan Kettering Single Cell Sequencing Initiative, to J.F. from the Care-for-Rare Foundation and the German Research Foundation (DFG), to C.A. from La Caixa foundation and a Harold E. Varmus graduate student fellowship from the Gerstner Sloan Kettering graduate school, to F.M.B. from a GMTEC Postdoctoral Research Fellowship and a MSKCC TROT Postdoctoral Fellowship (NIH T32CA160001), to K.M.T. from The Jane Coffin Childs Memorial Fund for Medical Research, and to F.J.S-R from HHMI (Hanna Gray Fellowship).

AUTHOR CONTRIBUTIONS

J.L. and M.R. conceived the project, performed and analyzed experiments, and wrote the paper with assistance from all authors. Z.C. conceived the project and performed and analyzed experiments. J.F., T.H., F.M.B., K.M.T., L.Z., C.A., K.R., N.S.R., S.T., F.S.R., and L.E.D. performed and analyzed experiments or provided key reagents. Y.H., T.B., and S.T. assisted with library preparation and analysis of RNA-seq data. A.K., F.J.S-R, and E.d.S. performed and analyzed *in vivo* experiments. M.Z. and C.A.S. supervised experiments and provided tissue specimens. J.W. provided pathological analysis of mouse and human tissue sections. W.A. provided and analyzed patient data. C.L.S. and S.W.L. conceived the project, supervised experiments, and wrote the paper.

REFERENCES

1. Siegel RL, Miller KD, Jemal A. Cancer statistics, 2018. CA Cancer J Clin **2018**;68(1):7-30 doi 10.3322/caac.21442.

2. Huggins C. Control of cancers of man by endocrinologic methods. Cancer Res **1957**;17(5):467-72.

3. Abida W, Cyrta J, Heller G, Prandi D, Armenia J, Coleman I*, et al.* Genomic correlates of clinical outcome in advanced prostate cancer. Proc Natl Acad Sci U S A **2019**;116(23):11428-36 doi 10.1073/pnas.1902651116.

4. Robinson D, Van Allen EM, Wu YM, Schultz N, Lonigro RJ, Mosquera JM*, et al.* Integrative Clinical Genomics of Advanced Prostate Cancer. Cell **2015**;162(2):454 doi 10.1016/j.cell.2015.06.053.

5. Abida W, Armenia J, Gopalan A, Brennan R, Walsh M, Barron D*, et al.* Prospective Genomic Profiling of Prostate Cancer Across Disease States Reveals Germline and Somatic Alterations That May Affect Clinical Decision Making. JCO Precis Oncol **2017**;2017 doi 10.1200/PO.17.00029.

6. Armenia J, Wankowicz SAM, Liu D, Gao J, Kundra R, Reznik E*, et al.* The long tail of oncogenic drivers in prostate cancer. Nat Genet **2018**;50(5):645-51 doi 10.1038/s41588-018-0078-z.

7. Sun Y, Campisi J, Higano C, Beer TM, Porter P, Coleman I*, et al.* Treatment-induced damage to the tumor microenvironment promotes prostate cancer therapy resistance through WNT16B. Nat Med **2012**;18(9):1359-68 doi 10.1038/nm.2890.

8. Gurel B, Iwata T, Koh CM, Jenkins RB, Lan F, Van Dang C*, et al.* Nuclear MYC protein overexpression is an early alteration in human prostate carcinogenesis. Mod Pathol **2008**;21(9):1156-67 doi 10.1038/modpathol.2008.111.

9. Arriaga JM, Abate-Shen C. Genetically Engineered Mouse Models of Prostate Cancer in the Postgenomic Era. Cold Spring Harb Perspect Med **2019**;9(2) doi 10.1101/cshperspect.a030528.

10. Choi HJ, Lee HB, Jung S, Park HK, Jo W, Cho SM*, et al.* Development of a Mouse Model of Prostate Cancer Using the Sleeping Beauty Transposon and Electroporation. Molecules **2018**;23(6) doi 10.3390/molecules23061360.

11. Maresch R, Mueller S, Veltkamp C, Ollinger R, Friedrich M, Heid I*, et al.* Multiplexed pancreatic genome engineering and cancer induction by transfection-based CRISPR/Cas9 delivery in mice. Nat Commun **2016**;7:10770 doi 10.1038/ncomms10770.

12. Park JS, Lim KM, Park SG, Jung SY, Choi HJ, Lee DH*, et al.* Pancreatic cancer induced by in vivo electroporation-enhanced sleeping beauty transposon gene delivery system in mouse. Pancreas **2014**;43(4):614-8 doi 10.1097/MPA.0000000000000102.

13. Seehawer M, Heinzmann F, D'Artista L, Harbig J, Roux PF, Hoenicke L*, et al.* Necroptosis microenvironment directs lineage commitment in liver cancer. Nature **2018**;562(7725):69-75 doi 10.1038/s41586-018-0519-y.

14. Hubbard GK, Mutton LN, Khalili M, McMullin RP, Hicks JL, Bianchi-Frias D*, et al.* Combined MYC Activation and Pten Loss Are Sufficient to Create Genomic Instability and Lethal Metastatic Prostate Cancer. Cancer Res **2016**;76(2):283-92 doi 10.1158/0008-5472.CAN-14-3280.

15. Kim J, Eltoum IE, Roh M, Wang J, Abdulkadir SA. Interactions between cells with distinct mutations in c-MYC and Pten in prostate cancer. PLoS Genet **2009**;5(7):e1000542 doi 10.1371/journal.pgen.1000542.

16. Grasso CS, Wu YM, Robinson DR, Cao X, Dhanasekaran SM, Khan AP*, et al.* The mutational landscape of lethal castration-resistant prostate cancer. Nature **2012**;487(7406):239-43 doi 10.1038/nature11125.

17. De Laere B, Oeyen S, Mayrhofer M, Whitington T, van Dam PJ, Van Oyen P*, et al.* TP53 Outperforms Other Androgen Receptor Biomarkers to Predict Abiraterone or Enzalutamide Outcome in Metastatic Castration-Resistant Prostate Cancer. Clin Cancer Res **2019**;25(6):1766-73 doi 10.1158/1078-0432.CCR-18-1943.

18. Bluemn EG, Coleman IM, Lucas JM, Coleman RT, Hernandez-Lopez S, Tharakan R*, et al.* Androgen Receptor Pathway-Independent Prostate Cancer Is Sustained through FGF Signaling. Cancer Cell **2017**;32(4):474-89 e6 doi 10.1016/j.ccell.2017.09.003.

19. Kumar A, Coleman I, Morrissey C, Zhang X, True LD, Gulati R*, et al.* Substantial interindividual and limited intraindividual genomic diversity among tumors from men with metastatic prostate cancer. Nat Med **2016**;22(4):369-78 doi 10.1038/nm.4053.

20. Chen WS, Aggarwal R, Zhang L, Zhao SG, Thomas GV, Beer TM*, et al.* Genomic Drivers of Poor Prognosis and Enzalutamide Resistance in Metastatic Castration-resistant Prostate Cancer. Eur Urol **2019**;76(5):562-71 doi 10.1016/j.eururo.2019.03.020.

21. Watson PA, Ellwood-Yen K, King JC, Wongvipat J, Lebeau MM, Sawyers CL. Context-dependent hormone-refractory progression revealed through characterization of a novel murine prostate cancer cell line. Cancer Res **2005**;65(24):11565-71 doi 10.1158/0008-5472.CAN-05-3441.

22. Ellwood-Yen K, Graeber TG, Wongvipat J, Iruela-Arispe ML, Zhang J, Matusik R*, et al.* Myc-driven murine prostate cancer shares molecular features with human prostate tumors. Cancer Cell **2003**;4(3):223-38.

23. Shlien A, Tabori U, Marshall CR, Pienkowska M, Feuk L, Novokmet A*, et al.* Excessive genomic DNA copy number variation in the Li-Fraumeni cancer predisposition syndrome. Proc Natl Acad Sci U S A **2008**;105(32):11264-9 doi 10.1073/pnas.0802970105.

24. Ciriello G, Miller ML, Aksoy BA, Senbabaoglu Y, Schultz N, Sander C. Emerging landscape of oncogenic signatures across human cancers. Nat Genet **2013**;45(10):1127-33 doi 10.1038/ng.2762.

25. Quigley DA, Dang HX, Zhao SG, Lloyd P, Aggarwal R, Alumkal JJ*, et al.* Genomic Hallmarks and Structural Variation in Metastatic Prostate Cancer. Cell **2018**;174(3):758-69 e9 doi 10.1016/j.cell.2018.06.039.

26. Hieronymus H, Schultz N, Gopalan A, Carver BS, Chang MT, Xiao Y*, et al.* Copy number alteration burden predicts prostate cancer relapse. Proc Natl Acad Sci U S A **2014**;111(30):11139-44 doi 10.1073/pnas.1411446111.

27. Ouyang X, Jessen WJ, Al-Ahmadie H, Serio AM, Lin Y, Shih WJ*, et al.* Activator protein-1 transcription factors are associated with progression and recurrence of prostate cancer. Cancer Res **2008**;68(7):2132-44 doi 10.1158/0008-5472.CAN-07-6055.

28. Visakorpi T, Hyytinen E, Koivisto P, Tanner M, Keinanen R, Palmberg C*, et al.* In vivo amplification of the androgen receptor gene and progression of human prostate cancer. Nat Genet **1995**;9(4):401-6 doi 10.1038/ng0495-401.

29. Logan CY, Nusse R. The Wnt signaling pathway in development and disease. Annu Rev Cell Dev Biol **2004**;20:781-810 doi 10.1146/annurev.cellbio.20.010403.113126.

30. Hausmann G, Banziger C, Basler K. Helping Wingless take flight: how WNT proteins are secreted. Nat Rev Mol Cell Biol **2007**;8(4):331-6 doi 10.1038/nrm2141.

31. Cancer Genome Atlas Research N. The Molecular Taxonomy of Primary Prostate Cancer. Cell **2015**;163(4):1011-25 doi 10.1016/j.cell.2015.10.025.

32. Montanari M, Rossetti S, Cavaliere C, D'Aniello C, Malzone MG, Vanacore D*, et al.* Epithelial-mesenchymal transition in prostate cancer: an overview. Oncotarget **2017**;8(21):35376-89 doi 10.18632/oncotarget.15686.

33. Stylianou N, Lehman ML, Wang C, Fard AT, Rockstroh A, Fazli L*, et al.* A molecular portrait of epithelial-mesenchymal plasticity in prostate cancer associated with clinical outcome. Oncogene **2019**;38(7):913-34 doi 10.1038/s41388-018-0488-5.

34. Reya T, Clevers H. Wnt signalling in stem cells and cancer. Nature **2005**;434(7035):843-50 doi 10.1038/nature03319.

35. Barker N, Clevers H. Mining the Wnt pathway for cancer therapeutics. Nat Rev Drug Discov **2006**;5(12):997-1014 doi 10.1038/nrd2154.

36. Huang SM, Mishina YM, Liu S, Cheung A, Stegmeier F, Michaud GA*, et al.* Tankyrase inhibition stabilizes axin and antagonizes Wnt signalling. Nature **2009**;461(7264):614-20 doi 10.1038/nature08356.

37. Ferri M, Liscio P, Carotti A, Asciutti S, Sardella R, Macchiarulo A*, et al.* Targeting Wnt-driven cancers: Discovery of novel tankyrase inhibitors. Eur J Med Chem **2017**;142:506-22 doi 10.1016/j.ejmech.2017.09.030.

38. Waaler J, Machon O, Tumova L, Dinh H, Korinek V, Wilson SR*, et al.* A novel tankyrase inhibitor decreases canonical Wnt signaling in colon carcinoma cells and reduces tumor growth in conditional APC mutant mice. Cancer Res **2012**;72(11):2822-32 doi 10.1158/0008-5472.CAN-11-3336.

39. Schatoff EM, Goswami S, Zafra MP, Foronda M, Shusterman M, Leach BI*, et al.* Distinct Colorectal Cancer-Associated APC Mutations Dictate Response to Tankyrase Inhibition. Cancer Discov **2019**;9(10):1358-71 doi 10.1158/2159-8290.CD-19-0289.

40. Roper J, Tammela T, Cetinbas NM, Akkad A, Roghanian A, Rickelt S, *et al.* In vivo genome editing and organoid transplantation models of colorectal cancer and metastasis. Nat Biotechnol **2017**;35(6):569-76 doi 10.1038/nbt.3836.

41. Sanchez-Rivera FJ, Papagiannakopoulos T, Romero R, Tammela T, Bauer MR, Bhutkar A, *et al.* Rapid modelling of cooperating genetic events in cancer through somatic genome editing. Nature **2014**;516(7531):428-31 doi 10.1038/nature13906.

42. Cho H, Herzka T, Zheng W, Qi J, Wilkinson JE, Bradner JE, *et al.* RapidCaP, a novel GEM model for metastatic prostate cancer analysis and therapy, reveals myc as a driver of Pten-mutant metastasis. Cancer Discov **2014**;4(3):318-33 doi 10.1158/2159-8290.CD-13-0346.

43. O'Rourke KP, Loizou E, Livshits G, Schatoff EM, Baslan T, Manchado E, *et al.* Transplantation of engineered organoids enables rapid generation of metastatic mouse models of colorectal cancer. Nat Biotechnol **2017**;35(6):577-82 doi 10.1038/nbt.3837.

44. Boj SF, Hwang CI, Baker LA, Chio, II, Engle DD, Corbo V, *et al.* Organoid models of human and mouse ductal pancreatic cancer. Cell **2015**;160(1-2):324-38 doi 10.1016/j.cell.2014.12.021.

45. Saborowski M, Saborowski A, Morris JPt, Bosbach B, Dow LE, Pelletier J, *et al.* A modular and flexible ESC-based mouse model of pancreatic cancer. Genes Dev **2014**;28(1):85-97 doi 10.1101/gad.232082.113.

46. Zuber J, Radtke I, Pardee TS, Zhao Z, Rappaport AR, Luo W, *et al.* Mouse models of human AML accurately predict chemotherapy response. Genes Dev **2009**;23(7):877-89 doi 10.1101/gad.1771409.

47. Kang TW, Yevsa T, Woller N, Hoenicke L, Wuestefeld T, Dauch D, *et al.* Senescence surveillance of pre-malignant hepatocytes limits liver cancer development. Nature **2011**;479(7374):547-51 doi 10.1038/nature10599.

48. Hickman MA, Malone RW, Lehmann-Bruinsma K, Sih TR, Knoell D, Szoka FC, *et al.* Gene expression following direct injection of DNA into liver. Hum Gene Ther **1994**;5(12):1477-83 doi 10.1089/hum.1994.5.12-1477.

49. Jefferies MT, Cox AC, Shorning BY, Meniel V, Griffiths D, Kynaston HG, *et al.* PTEN loss and activation of K-RAS and beta-catenin cooperate to accelerate prostate tumourigenesis. J Pathol **2017**;243(4):442-56 doi 10.1002/path.4977.

50. Lee SH, Luong R, Johnson DT, Cunha GR, Rivina L, Gonzalgo ML, *et al.* Androgen signaling is a confounding factor for beta-catenin-mediated prostate tumorigenesis. Oncogene **2016**;35(6):702-14 doi 10.1038/onc.2015.117.

51. Wellenstein MD, Coffelt SB, Duits DEM, van Miltenburg MH, Slagter M, de Rink I, *et al.* Loss of p53 triggers WNT-dependent systemic inflammation to drive breast cancer metastasis. Nature **2019**;572(7770):538-42 doi 10.1038/s41586-019-1450-6.

52. Ruscetti M, Quach B, Dadashian EL, Mulholland DJ, Wu H. Tracking and Functional Characterization of Epithelial-Mesenchymal Transition and Mesenchymal Tumor Cells during Prostate Cancer Metastasis. Cancer Res **2015**;75(13):2749-59 doi 10.1158/0008-5472.CAN-14-3476.

53. Chicas A, Wang X, Zhang C, McCurrach M, Zhao Z, Mert O*, et al.* Dissecting the unique role of the retinoblastoma tumor suppressor during cellular senescence. Cancer Cell **2010**;17(4):376-87 doi 10.1016/j.ccr.2010.01.023.

54. Chien Y, Scuoppo C, Wang X, Fang X, Balgley B, Bolden JE*, et al.* Control of the senescence-associated secretory phenotype by NF-kappaB promotes senescence and enhances chemosensitivity. Genes Dev **2011**;25(20):2125-36 doi 10.1101/gad.17276711.

55. Drost J, Karthaus WR, Gao D, Driehuis E, Sawyers CL, Chen Y*, et al.* Organoid culture systems for prostate epithelial and cancer tissue. Nat Protoc **2016**;11(2):347-58 doi 10.1038/nprot.2016.006.

56. Schatoff EM, Zafra MP, Dow LE. Base editing the mammalian genome. Methods **2019**;164-165:100-8 doi 10.1016/j.ymeth.2019.02.022.

57. Adams EJ, Karthaus WR, Hoover E, Liu D, Gruet A, Zhang Z*, et al.* FOXA1 mutations alter pioneering activity, differentiation and prostate cancer phenotypes. Nature **2019**;571(7765):408-12 doi 10.1038/s41586-019-1318-9.

58. Wu X, Wu J, Huang J, Powell WC, Zhang J, Matusik RJ*, et al.* Generation of a prostate epithelial cell-specific Cre transgenic mouse model for tissue-specific gene ablation. Mech Dev **2001**;101(1-2):61-9.

59. Dow LE, Nasr Z, Saborowski M, Ebbesen SH, Manchado E, Tasdemir N*, et al.* Conditional reverse tet-transactivator mouse strains for the efficient induction of TRE-regulated transgenes in mice. PLoS One **2014**;9(4):e95236 doi 10.1371/journal.pone.0095236.

60. Ruscetti M, Dadashian EL, Guo W, Quach B, Mulholland DJ, Park JW*, et al.* HDAC inhibition impedes epithelial-mesenchymal plasticity and suppresses metastatic, castration-resistant prostate cancer. Oncogene **2016**;35(29):3781-95 doi 10.1038/onc.2015.444.

61. Bolger AM, Lohse M, Usadel B. Trimmomatic: a flexible trimmer for Illumina sequence data. Bioinformatics **2014**;30(15):2114-20 doi 10.1093/bioinformatics/btu170.

62. Dobin A, Davis CA, Schlesinger F, Drenkow J, Zaleski C, Jha S*, et al.* STAR: ultrafast universal RNA-seq aligner. Bioinformatics **2013**;29(1):15-21 doi 10.1093/bioinformatics/bts635.

63. Anders S, Pyl PT, Huber W. HTSeq--a Python framework to work with high-throughput sequencing data. Bioinformatics **2015**;31(2):166-9 doi 10.1093/bioinformatics/btu638.

64. Love MI, Huber W, Anders S. Moderated estimation of fold change and dispersion for RNA-seq data with DESeq2. Genome Biol **2014**;15(12):550 doi 10.1186/s13059-014-0550-8.

65. Kuleshov MV, Jones MR, Rouillard AD, Fernandez NF, Duan Q, Wang Z*, et al.* Enrichr: a comprehensive gene set enrichment analysis web server 2016 update. Nucleic Acids Res **2016**;44(W1):W90-7 doi 10.1093/nar/gkw377.

66. Baslan T, Kendall J, Rodgers L, Cox H, Riggs M, Stepansky A*, et al.* Genome-wide copy number analysis of single cells. Nat Protoc **2012**;7(6):1024-41 doi 10.1038/nprot.2012.039.

67. Baslan T, Kendall J, Ward B, Cox H, Leotta A, Rodgers L, *et al.* Optimizing sparse sequencing of single cells for highly multiplex copy number profiling. Genome Res **2015**;25(5):714-24 doi 10.1101/gr.188060.114.

68. Won HH, Scott SN, Brannon AR, Shah RH, Berger MF. Detecting somatic genetic alterations in tumor specimens by exon capture and massively parallel sequencing. J Vis Exp **2013**(80):e50710 doi 10.3791/50710.

69. DePristo MA, Banks E, Poplin R, Garimella KV, Maguire JR, Hartl C, *et al.* A framework for variation discovery and genotyping using next-generation DNA sequencing data. Nat Genet **2011**;43(5):491-8 doi 10.1038/ng.806.

70. Cibulskis K, Lawrence MS, Carter SL, Sivachenko A, Jaffe D, Sougnez C, *et al.* Sensitive detection of somatic point mutations in impure and heterogeneous cancer samples. Nat Biotechnol **2013**;31(3):213-9 doi 10.1038/nbt.2514.

71. Sanchez-Vega F, Mina M, Armenia J, Chatila WK, Luna A, La KC, *et al.* Oncogenic Signaling Pathways in The Cancer Genome Atlas. Cell **2018**;173(2):321-37 e10 doi 10.1016/j.cell.2018.03.035.

72. Zehir A, Benayed R, Shah RH, Syed A, Middha S, Kim HR, *et al.* Mutational landscape of metastatic cancer revealed from prospective clinical sequencing of 10,000 patients. Nat Med **2017**;23(6):703-13 doi 10.1038/nm.4333.

FIGURE LEGENDS

Figure 1. Somatic induction of oncogenic lesions by *in vivo* electroporation of the prostate gland

(A) Schematic of the electroporation-induced genetically engineered mouse model (EPO-GEMM) of prostate cancer. A *MYC* transposon vector in combination with a Sleeping Beauty transposase (SB13) and/or a CRISPR/Cas9 vector targeting *Pten (sgPten)* were delivered into the prostate by direct *in vivo* electroporation.

(B) Kaplan-Meier survival curve of C57BL/6 mice electroporated with a *MYC* transposon vector and a Sleeping Beauty transposase (*MYC*; black), a CRISPR/Cas9 vector targeting *Pten* (sg*Pten*; orange), or the combination of all vectors (*MYC* sg*Pten*; blue).

(C) Representative hematoxylin and eosin (H&E) and immunohistochemical staining of a well differentiated *MPt* EPO-GEMM (top) or $Nkx3.1^{CreERT2/+}$;$Pten^{fl/fl}$;*ARR2/Pbsn-MYC* ($NP^{Hi}MYC$) classic GEMM prostate tumor (bottom).

(D) Representative H&E and immunohistochemical staining of a poorly differentiated *MPt* EPO-GEMM (top) or $NP^{Hi}MYC$ classic GEMM prostate tumor (bottom).

Figure 2. Engineering advanced prostate cancer *de novo* using EPO-GEMMs

(A) Kaplan-Meier survival curve of mice electroporated with the *MYC* transposon vector and a Sleeping Beauty transposase (*MYC*; black), a CRISPR/Cas9 vector targeting *p53* (sg*p53*; orange), or all vectors (*MYC* sg*p53*; green).

(B) Representative H&E staining of liver and lungs isolated from mice with *MYC;sgp53* (*MP*) EPO-GEMM prostate tumors. Arrows, metastatic nodules.

(C) Representative H&E and immunohistochemical staining of a *MP* EPO-GEMM prostate tumor (left) and a corresponding liver metastasis (right).

(D) IC_{50} values for enzalutamide in indicated murine and human prostate cancer cell lines (n=3; error bars, mean ± s.e.m; **** $p < 0.0001$; One-way ANOVA).

(E) Change in tumor volume of *MP* EPO-GEMM prostate tumors in intact or castrated (CX) mice one-week post-surgery (n=3-10; error bars, mean ± s.e.m; unpaired two-tailed t test).

(F) Frequency plot of copy number variation (CNV) analysis of *MP* (n=19) and *MPt* (n=11 (from 6 tumors)) EPO-GEMM prostate tumors.

Figure 3. A subset of MYC/p53-driven tumors acquire WNT pathway activation.

(A) Principle component analysis (PCA) of the transcriptional output of *MP* EPO-GEMM prostate tumors (n=10) compared to wild type (WT) (n=6) murine prostate tissue. *MP* tumors segregate into two clusters (group 1 and group 2).

(B) Gene set enrichment analysis (GSEA) of group 1 and group 2 clusters of *MP* prostate tumors from (A) reveals an enrichment for β-catenin signaling in one of the populations (hereafter *MP* WNT^{hi}).

(C) Heat map of WNT pathway gene expression in *MP* WNT^{hi} and *MP* WNT^{lo} *MP* prostate tumors (n=5).

(D) Frequency of metastases in the liver in cohorts of mice with either *MP* WNT^{hi} or *MP* WNT^{lo} prostate tumors (n=5; two-sided Fisher's exact test).

(E) Representative immunohistochemical staining of *MP* WNT^{hi} and *MP* WNT^{lo} EPO-GEMM prostate tumors.

(F) Close up views of clonal CNVs in WNT pathway genes *Lrp6* (left) or *Wnt2b* (right) in individual *MP* WNT^{hi} EPO-GEMM prostate tumors (see arrows).

(G) Diagram of the *Apc* gene and the position of a point mutation found in a *MP* WNT^{hi} EPO-GEMM prostate tumor.

Figure 4. WNT pathway alterations are associated with metastatic disease in patients with advanced prostate cancer

(A) Oncoprint displaying the genomic status of *LRP5* or *LRP6* in prostate cancer patient samples isolated from either primary tumors (TCGA dataset (31)) or from metastatic sites (SU2C datasets (3,4)).

(B) Frequency of *LRP5* or *LRP6* amplifications in the same cohorts of patients as in (A) (two-sided Fisher's exact test).

(C) Frequency of *TP53* alterations in patients with locoregional prostate cancer, metastatic but castration sensitive prostate cancer (mPC), or metastatic castration resistant prostate cancer (mCRPC) from datasets in (5) (ns, not significant; two-sided Fisher's exact test).

(D) Frequency of amplifications in *MYC* in the same cohorts of patients as in (C) (ns, not significant; two-sided Fisher's exact test).

(E) Frequency of activating mutations in the WNT pathway genes *APC* or *CTNNB1* (encoding β-catenin) in the same cohorts of patients as in (C) (ns, not significant; two-sided Fisher's exact test).

(F) Frequency of *TP53* alterations in prostate cancer patient samples isolated from either primary tumors (TCGA dataset (31)) or from metastatic sites (SU2C dataset (3,4)) (two-sided Fisher's exact test).

(G) Frequency of amplifications in *MYC* in the same cohorts of patients as in (F) (two-sided Fisher's exact test).

(H) Frequency of activating mutations in the WNT pathway genes *APC* or *CTNNB1* (encoding β-catenin) in the same cohorts of patients as in (F) (two-sided Fisher's exact test).

(I) Frequency of activating mutations in the WNT pathway genes *APC* or *CTNNB1* in patients with locoregional or metastatic prostate cancer (mPC and mCRPC combined) from the same cohorts of patients as in (C) (two-sided Fisher's exact test).

(J) Kaplan-Meier survival curve of patients with advanced prostate cancer with (red; n=47) or without (green; n=81) activating mutations in the WNT signaling pathway from the SU2C dataset (3) (log-rank test). Median survival in months (m) shown inset.

(K) Quantification of immunofluorescence staining for β-catenin in tumor microarrays (TMAs) containing prostate tumor specimens from patients with locoregional or metastatic disease. The percentage of samples that stained positive for β-catenin is shown (two-sided Fisher's exact test).

(L) Representative immunofluorescence staining for β-catenin in TMAs containing prostate tumor specimens from patients with locoregional or metastatic disease. Samples scored as 0 or 1 were considered negative, and those scored as 2 or 3 as positive for β-catenin expression.

Figure 5. WNT pathway activation promotes prostate cancer metastasis

(A) Representative H&E and immunohistochemical staining of a primary *MPApc* prostate tumor. Arrows, nuclear β-catenin localization.

(B) Frequency of mice with macrometastatic disease in cohorts with either *MP* or *MPApc* prostate EPO-GEMM tumors (one-sided Fisher's exact test).

(C) H&E staining of liver and lung metastases isolated from mice with *MPApc* EPO-GEMM prostate tumors. Arrows, metastatic nodules.

(D) Kaplan-Meier survival curve of mice with indicated EPO-GEMM prostate tumors (log-rank test).

(E) Representative immunohistochemical staining of primary *MP* and *MPApc* EPO-GEMM prostate tumors.

(F) Representative H&E and immunohistochemical staining of a primary *MPtApc* prostate tumor.

(G) Representative immunohistochemical staining of a primary *MPtApc* EPO-GEMM prostate tumor.

(H) H&E staining of a liver metastasis isolated from a mouse with a *MPtApc* EPO-GEMM prostate tumor.

(I) Frequency of mice with macrometastatic disease in cohorts with either *MPt* or *MPtApc* prostate EPO-GEMM tumors (one-sided Fisher's exact test).

Figure 6. *Apc* mutations drive disease and metastatic progression in prostate cancer organoid models

(A) Representative gross bright field (top) and H&E (bottom) images of prostates of NOD-*scid* IL2Rγ^{null} (NSG) mice 15 weeks after orthotopic transplantation of prostate organoids with indicated genotypes.

(B) Representative immunohistochemical staining of prostates of NSG mice 15 weeks after orthotopic transplantation of prostate organoids with indicated genotypes.

(C-D) Representative bioluminescence images of NSG mice 4 weeks after tail vein injection of mouse prostate organoids with indicated genotypes (n=3-4).

Figure 7. Targeting WNT signaling disrupts prostate cancer metastasis

(A) Growth assay of indicated mouse prostate cancer cell lines or primary murine fibroblasts treated with 1µM of tankyrase inhibitor G007-LK for 72 hours (n=2-3; error bars, mean ± s.e.m; One-way ANOVA). Growth is relative to treatment with vehicle control.

(B) Frequency of metastases in prostate tumor-bearing *MPApc* EPO-GEMM mice after treatment with the tankyrase inhibitor G007-LK (30 mg/kg body weight) or vehicle control (one-sided Fisher's exact test).

(C) Kaplan-Meier survival curve of prostate tumor-bearing *MPApc* EPO-GEMM mice treated as in (B) (log-rank test).

(D) Schematic of *in vivo* metastasis formation assay. *MPApc* prostate cancer cell lines were tail vein injected into *Nu/Nu* (Nude) mice and treatment with G007-LK or vehicle control initiated on the same day.

(E) Representative images of H&E stained livers isolated from mice after tail vein injection of *MPApc* prostate cancer cell lines and treatment with G007-LK (30mg/kg body weight) or vehicle control for 6 weeks (N, normal liver; T, tumor nodules).

(F) Frequency of liver metastases in mice after tail vein injection of *MPApc* prostate cancer cell lines and treatment as in (E) (one-sided Fisher's exact test).

(G) Schematic of orthotopic transplantation assay. *MP* $\mathrm{WNT}^{\mathrm{hi}}$ prostate cancer cells harboring a WNT reporter construct (7TCF-luciferase) were orthotopically transplanted into C57BL/6 mice. Treatment with G007-LK or vehicle control was initiated upon confirmation of tumor formation by luciferase imaging.

(H) Representative images of H&E stained livers isolated from mice after orthotopic injection of *MP* $\mathrm{WNT}^{\mathrm{hi}}$ prostate cancer cells and treatment with G007-LK (30mg/kg body weight) or vehicle control for 4 weeks. N, normal liver. Arrows, metastatic tumor nodules.

(I) Number of metastatic liver nodules in mice after orthotopic injection of *MP* $\mathrm{WNT}^{\mathrm{hi}}$ prostate cancer cells and treatment as in (H) (n=9-10; error bars, mean ± s.e.m; two-tailed Mann-Whitney test).

Figure 1: Somatic induction of oncogenic lesions by *in vivo* electroporation of the prostate gland

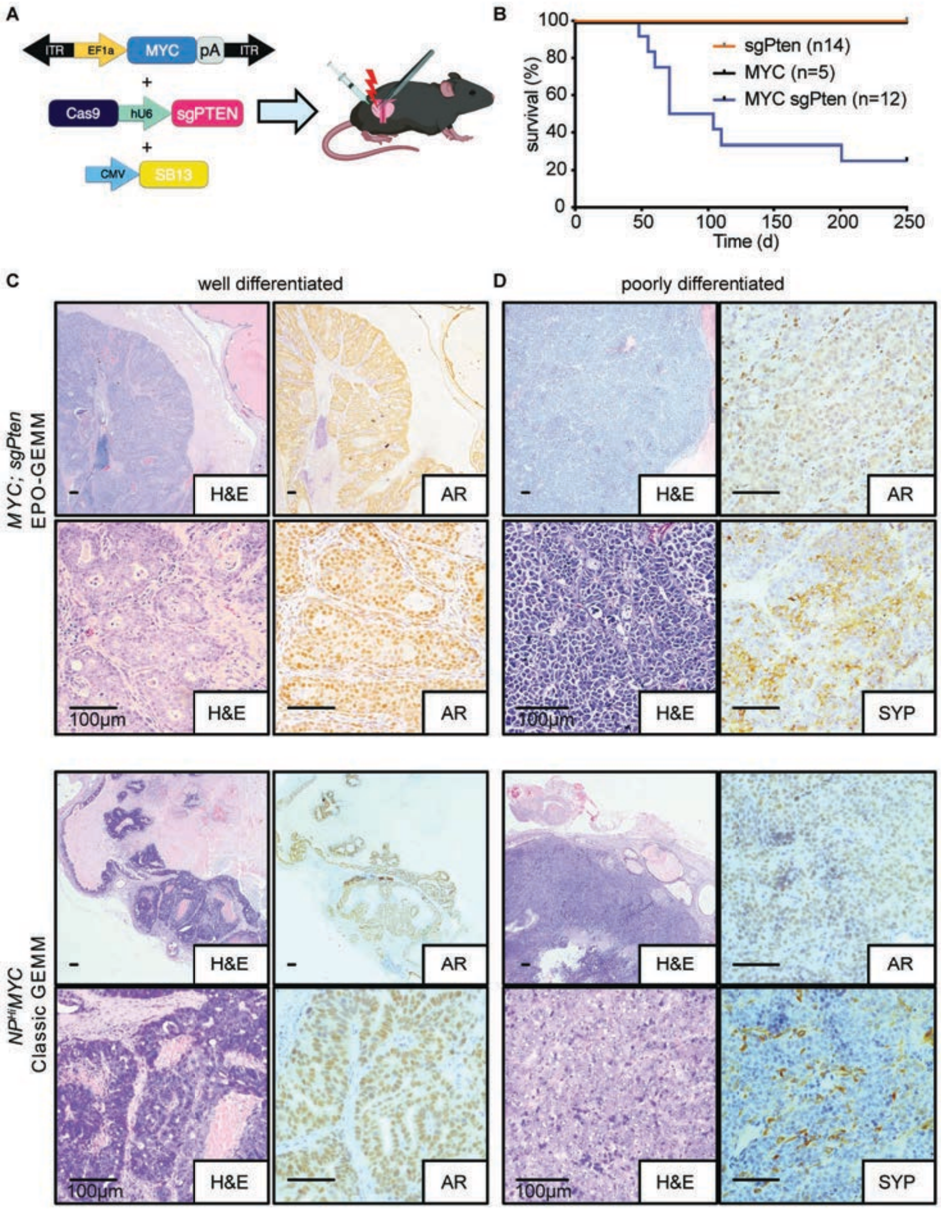

Figure 2: Engineering advanced prostate cancer *de novo* using EPO-GEMMs

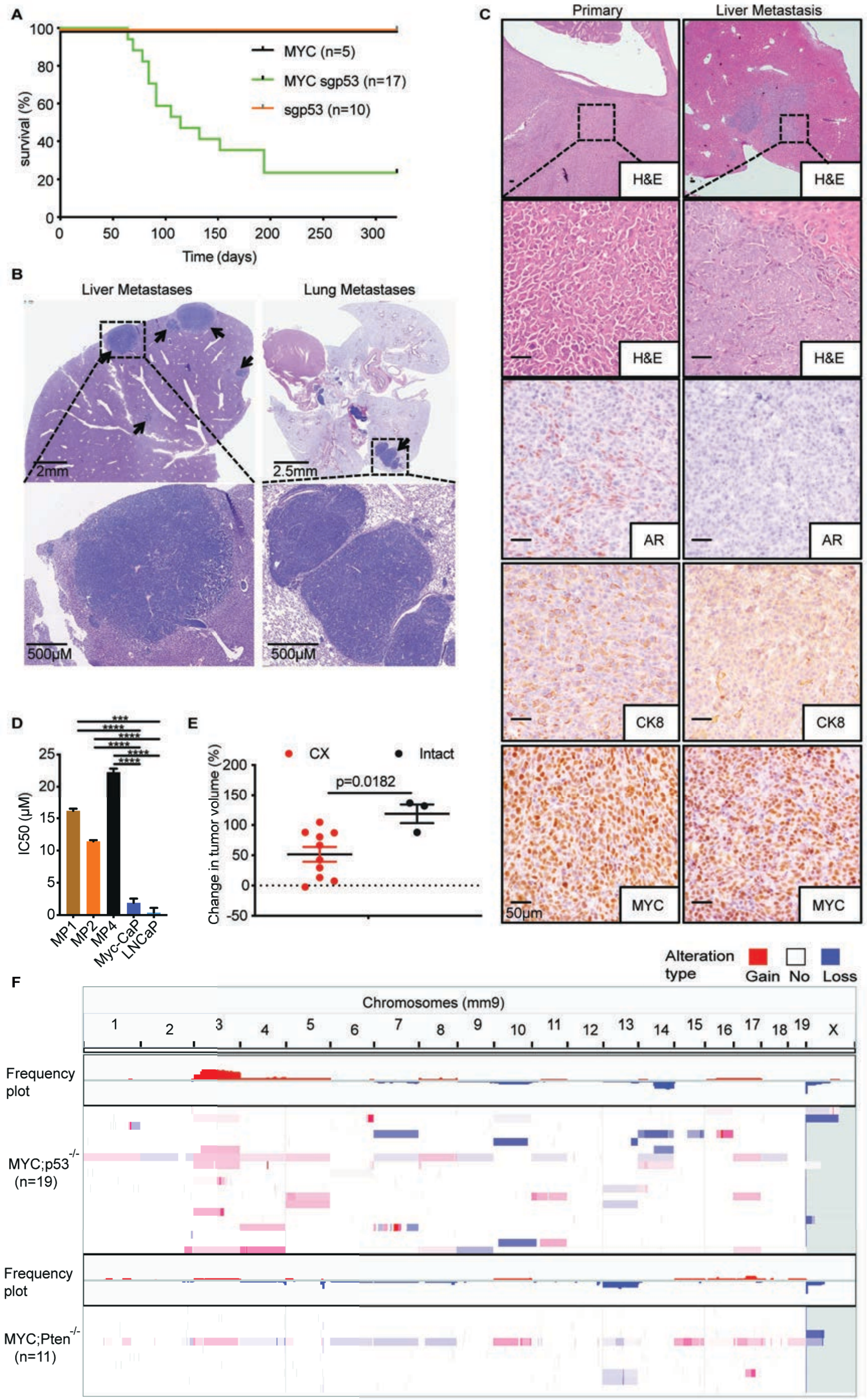

Figure 3: A subset of MYC/p53-driven tumors acquire WNT pathway activation

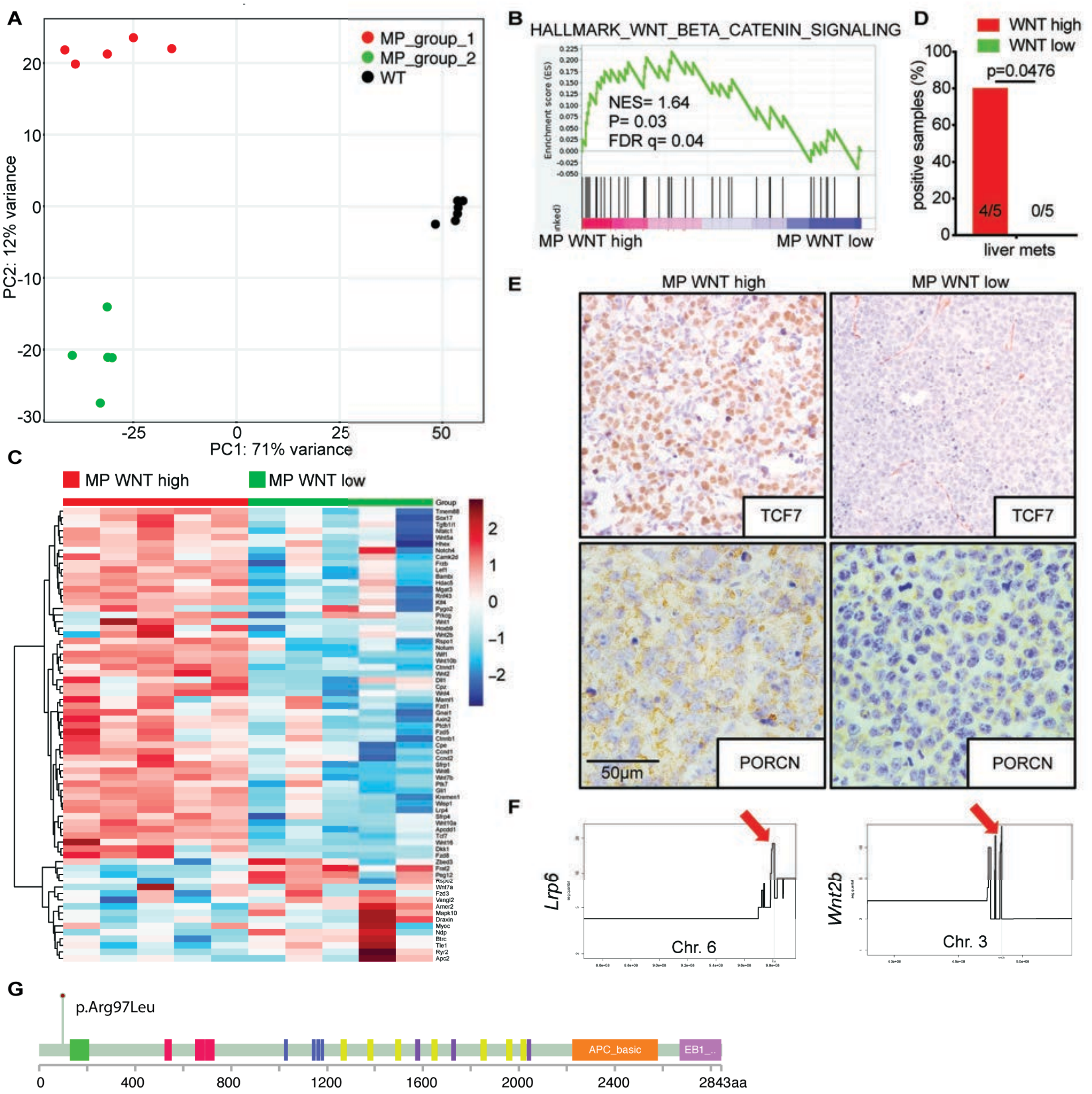

Figure 4. WNT pathway alterations are associated with metastatic disease in patients with advanced prostate cancer

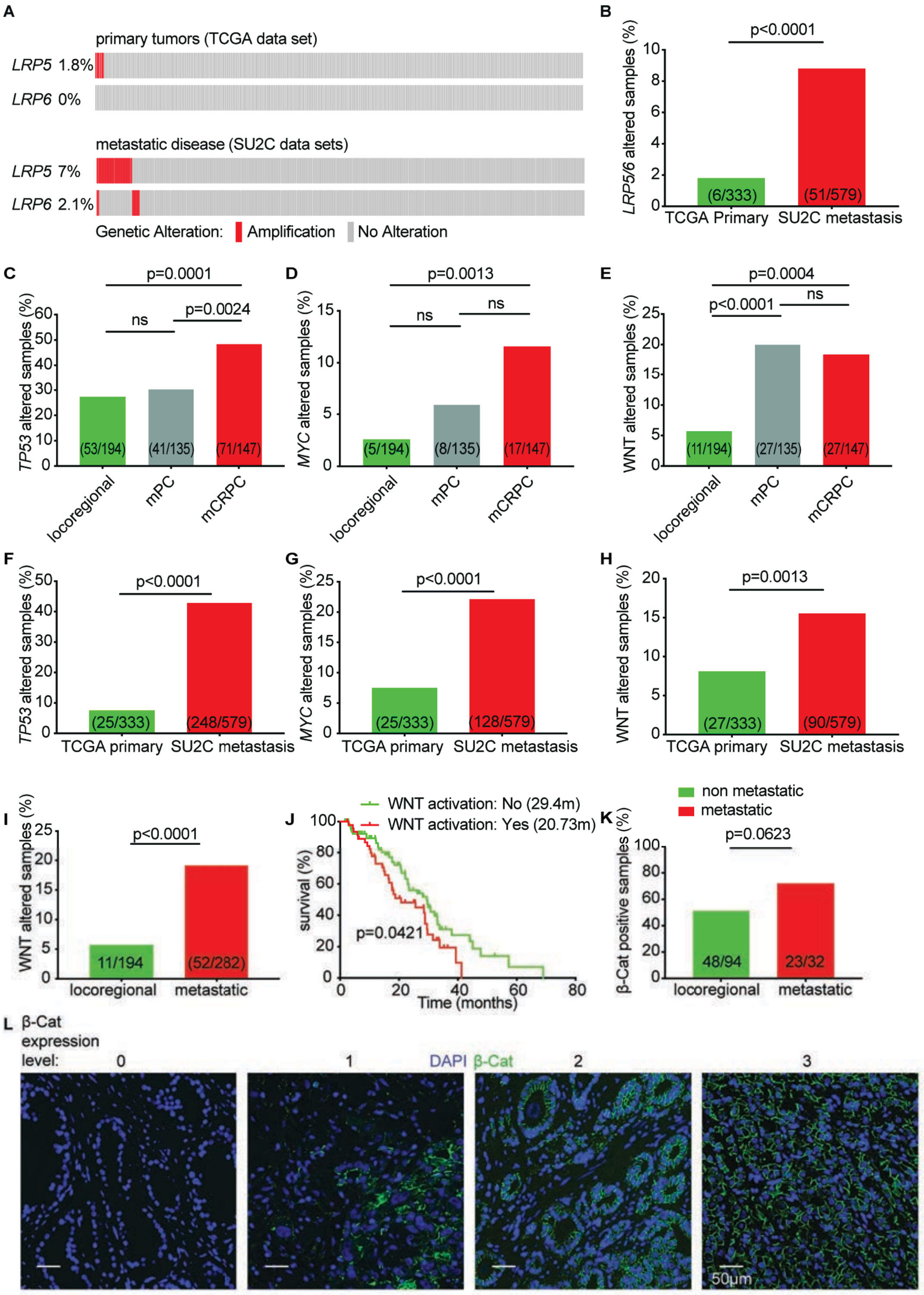

Figure 5: WNT pathway activation promotes prostate cancer metastasis

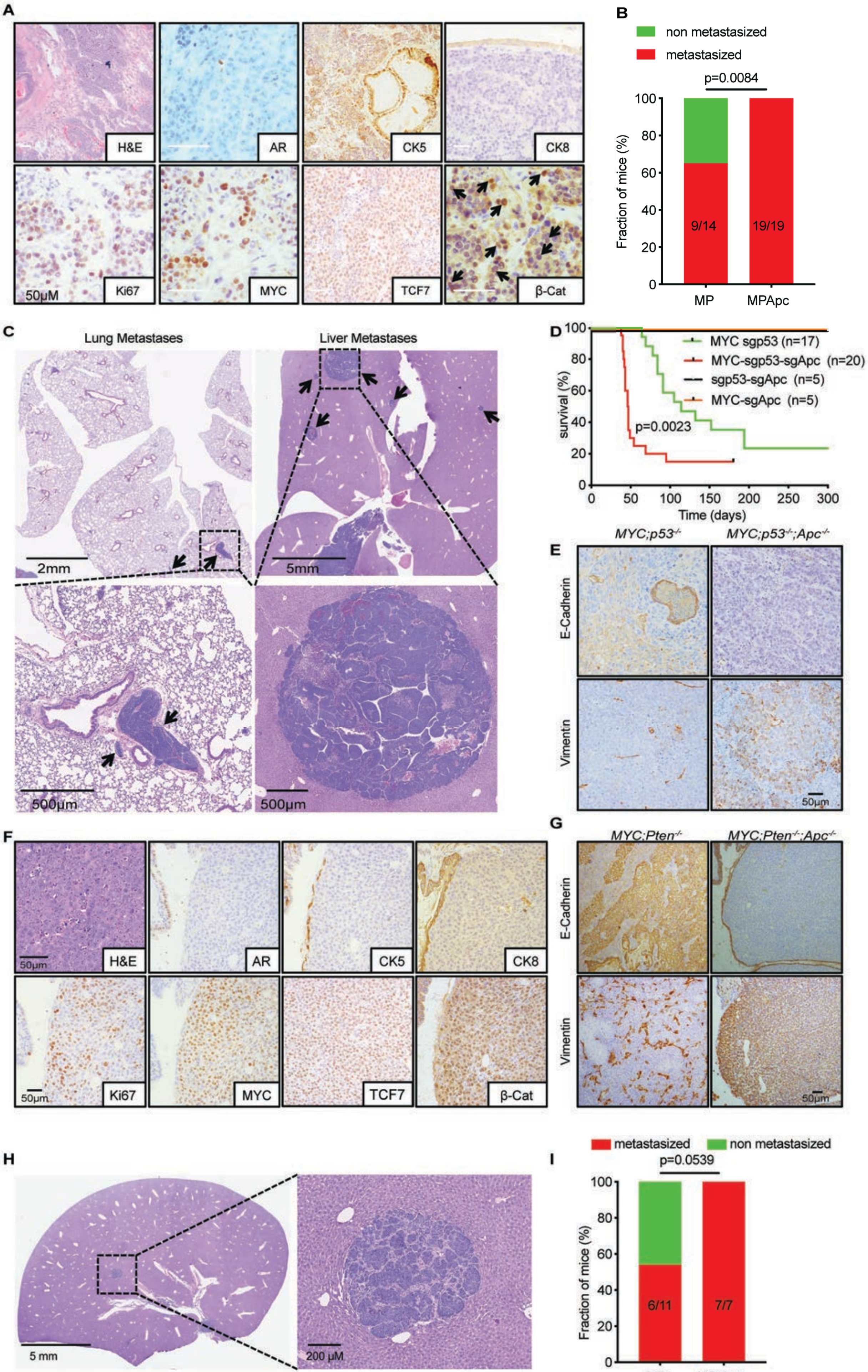

Figure 6: Apc mutations drive disease and metastatic progression in prostate cancer organoid models

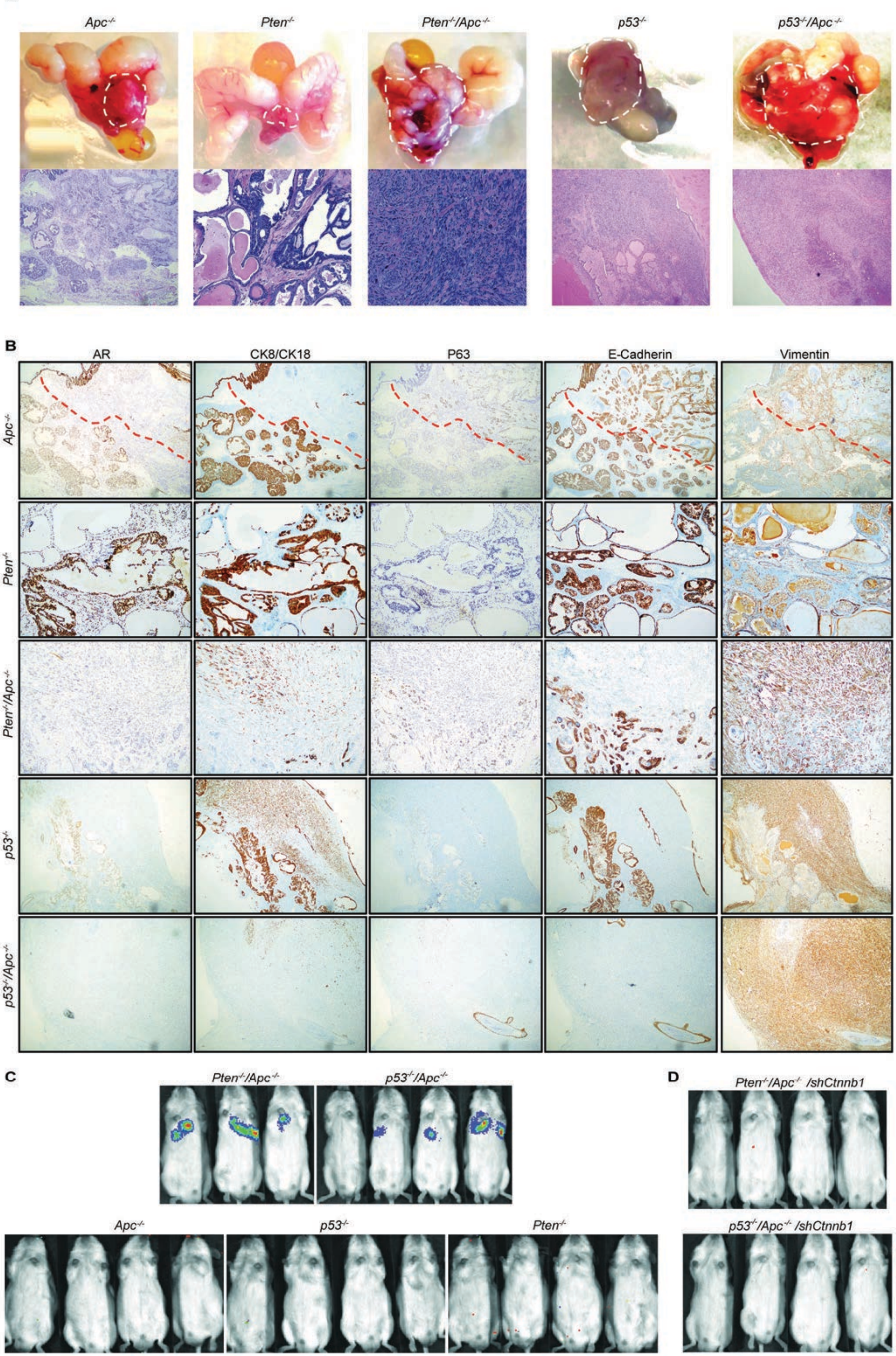

Figure 7: Targeting WNT signaling disrupts prostate cancer metastasis

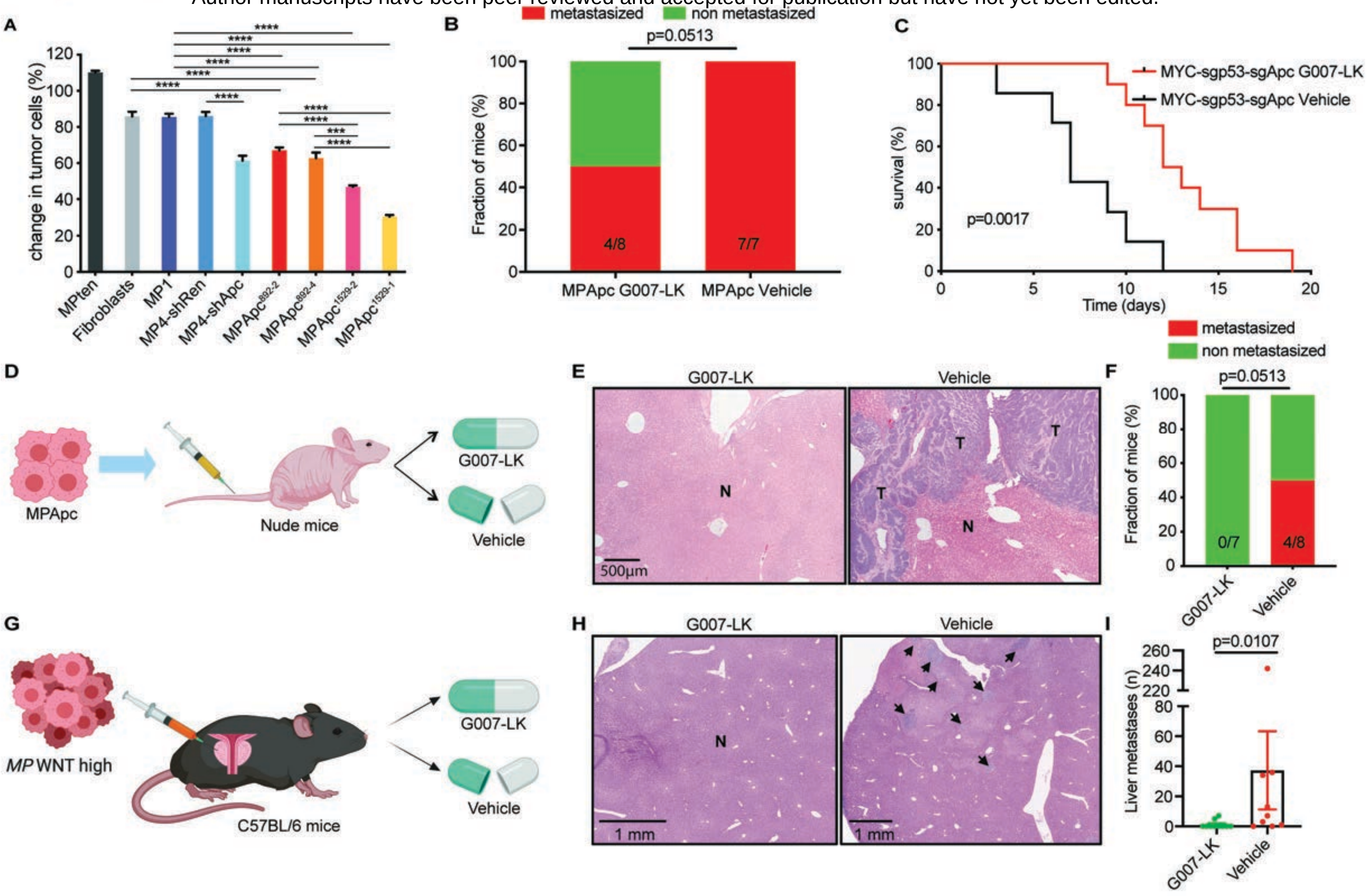

AACR American Association for Cancer Research

CANCER DISCOVERY

Somatic tissue engineering in mouse models reveals an actionable role for WNT pathway alterations in prostate cancer metastasis

Josef Leibold, Marcus Ruscetti, Zhen Cao, et al.

Cancer Discov Published OnlineFirst May 6, 2020.